Final Report (8/15/2006-8/14/2010)

During the reporting period we focused our attention on six projects: a) development of integrated MEMS Sierpinski antenna on low cost organic substrate; b) development of adaptive MEMS antenna on low cost organic substrate with UIUC; c) development of low cost packaging technique for RF MEMS switches on organic substrate; d) design of PZT MEMS switches and circuits in collaboration with ARL and hybrid integration on low cost organic substrates; e) development of a UWB elliptical monopole with a reconfigurable band notch utilizing integrated RF MEMS switches; f) development of low cost organic packaging for mm-wave integrated circuits. Details of each one of these projects are presented below.

1. Reconfigurable Sierpinski Antenna

1.1 Introduction

During this reporting period, our efforts were focused on the development of a MEMS reconfigurable Sierpinski antenna on LCP substrate. In this project, MEMS switches were used to sequentially activate and deactivate parts of a multiband antenna. The implementation of such a concept allows for the direct actuation of the electrostatic MEMS switches through the RF signal path, therefore eliminating the need for DC bias lines. The coplanar waveguide feed facilitates the antenna's fabrication and measurement setup. This reconfigurable antenna operates at several different frequencies while it maintains its radiation characteristics. Simulation and measurement results are presented with excellent agreement.

1.2 Implementation

The implementation of a sequentially-activated antenna is shown in Figure 1. All of the MEMS switches used are single-supported (cantilever-type) and ohmic. Regardless of the applied voltage, the triangular element that is closest to the RF/DC input is always active (Figure 2, State 1). When no DC voltage is applied, the antenna radiates at its highest frequency. When a low DC voltage is applied to the signal line, the first set of MEMS switches actuate and this activates the second level of triangular elements (Figure 2, State 2). The antenna now radiates at a lower frequency. Since all of the switches are ohmic, the low voltage is also present at the membrane of the next set of switches. However, these switches are designed to actuate at a higher voltage so they are unaffected by the voltage present. When a higher DC voltage is applied, the first set of MEMS switches remain “ON” while the second set of switches actuate (Figure 2, State 3). This activates the next iteration, consisting of six additional radiating elements. Again, this higher voltage is present at the next set of switch membranes, but the electrostatic force created is not sufficient for actuation. Finally, when the voltage is increased to its highest value, the first two sets of switches remain “ON” while the remaining set of switches actuates (Figure 2, State 4). In a way, the voltage cascades from one state to the next like a sequence of overflowing buckets. This technique could not be used if the switches were capacitive since they do not pass DC voltage. The four different states are illustrated in Figure 2, where all of the activated regions for different voltages are dark in color. This biasing technique allows for direct actuation of the electrostatic MEMS switches without the need for DC bias lines. The reduction or elimination of bias lines is highly advantageous because they can significantly distort the radiation patterns and they can introduce additional unwanted resonances.

LCP was chosen as the antenna substrate for its numerous advantages. LCP is a thin (100μm), flexible, low-loss ($\tan\delta \approx 0.004$), low moisture absorbing material with low-permittivity

($\varepsilon_r \approx 3$). Since the material is a polymer, there are additional packaging and cost advantages. All of these characteristics make it an ideal substrate for antennas, particularly at high frequencies. With respect to the geometry, the antenna elements have a 60^o flare angle and maintain the resonant structure's self-similarity with a log-periodicity of $\delta = 2$. The antenna is fed through a 6mm long CPW transmission line with a 50μm gap, a 1.3mm signal conductor width, and a 3μm thick gold layer. A picture of the fabricated antenna is shown in Figure 3. The overall size of the antenna, including the feed, is 20mm x 25mm. The coplanar waveguide feed was chosen to facilitate the measurement setup. This reconfigurable antenna operates at four different principle frequencies. For each of these frequencies, the antenna maintains its multiband performance.

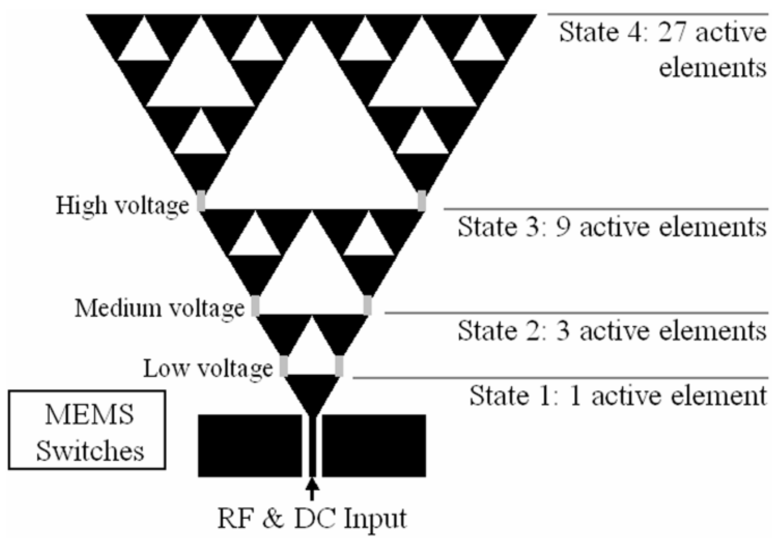

Fig. 1. Illustration of a MEMS reconfigurable Sierpinski antenna. The center line of the CPW feed provides the RF input and DC voltage for MEMS switch actuation.

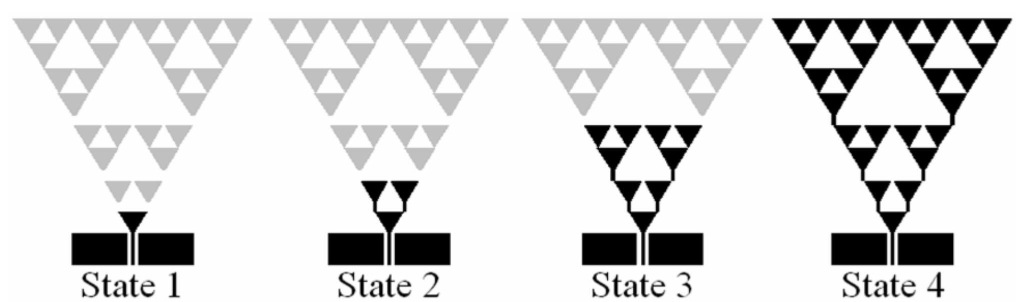

Fig. 2. The four different reconfigurable antenna states: State 1 has no voltage applied, State 2 has a low voltage applied, State 3 has a medium voltage applied, and State 4 has a high voltage applied. The activated (radiating) part of the antenna is darkened.

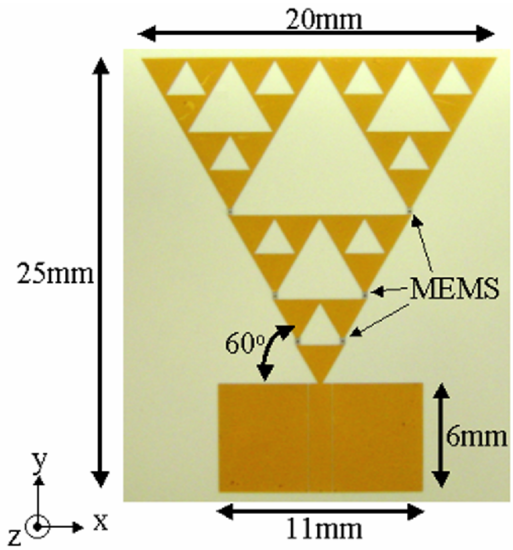

Fig. 3 Photo of the fabricated Sierpinski antenna with MEMS switches shown. The design parameters are labeled on the plot.

The placement of the RF MEMS switches was illustrated in Figure 1 and shown in Figure 10. In order to bias the ohmic switches for electrostatic actuation, the MEMS need to have an applied voltage. A metal pad beneath the switch should be present to attract the charged metal. The metal pad must be placed under a thin dielectric material (such as silicon nitride) to prevent direct metal bridge to metal pad contact. Otherwise, no charge will develop and the switch will not actuate. In this case, the pad is not connected to anything and is considered a floating ground. Traditionally, the actuation voltage is applied via a DC bias line. However, in order to prevent RF leakage into the DC path, careful attention needs to be given to the DC bias lines themselves. This can be implemented in different ways:

a) By using a quarter-wavelength transmission line connected to a quarter-wavelength open-circuit radial stub. Alternatively, a half-wavelength transmission line without a radial stub can be used with a reduced bandwidth. Each MEMS switch would require a different DC bias line and for this antenna that would require six lengthy metal lines being added. This would have a pronounced effect on the antenna performance. Therefore, this solution is not advisable.

b) High-resistance lines have been investigated to provide a wider bandwidth alternative. Aluminum doped Zinc Oxide (AZO) is one such example. Thin-films of this kind are generally deposited using Combustion Chemical Vapor Deposition (CCVD), which uses very high temperatures. This is not a problem for materials like silicon, but it is much higher than the melting point of the organic substrate (≈315^{o}C) used in this work. At the moment, very high resistivity materials that can be deposited at low temperature are not widely available but are under investigation.

The proposed alternative to these approaches is to eliminate the need for DC bias lines. Instead, the biasing is handled through the antenna structure itself. Here, the DC voltage and the RF signal are both applied to the antenna through the same signal conductor of the CPW feed line. The antenna reconfigurability is made possible by using MEMS switches of varying actuation voltages.

1.3 Antenna Results

The antenna reconfigurability was tested by varying the voltage and witnessing the antenna transition between the different states. The antenna was able to transition from the first to the last state and back again without a change in the performance. This procedure was repeated many times without problems. This demonstrates that the floating ground is sufficient.

The return loss measurements were taken with an Agilent 8510C vector network analyzer using 850µm pitch GSG RF probes. Pattern measurements were taken using an Agilent 8530 vector network analyzer with the antenna inside an anechoic chamber. End-launch gold SMA connectors were hand-soldered onto the antenna for pattern measurements. These connectors have a maximum operating frequency of 18 GHz, which coincides with the highest principle frequency of the antenna when no voltage is applied. Since the gap in the CPW lines is 50µm wide to achieve 50Ω for our chosen signal line width, manual soldering of the connector pin may not always result in a smooth transition. This can cause undesired ripple in the measurements at higher frequencies. The return loss measurement results are shown in Figure 4. The resonant frequencies roughly halve as the antenna increases in size. These measurement results are summarized in Table I and agree well with the simulated values.

.

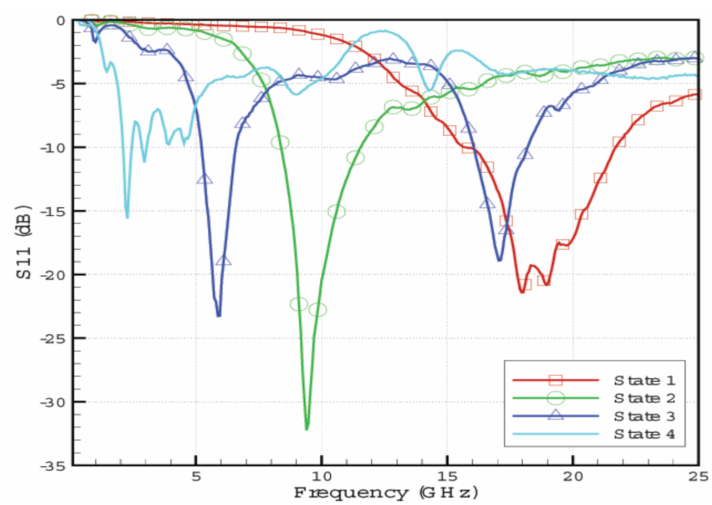

Fig. 4 Measured return loss for all four states of the designed reconfigurable antenna.

Table I
Tabulated antenna measurement results for all four states.
The actuation voltage and measured resonances are given.

State	Voltage	f_1	f_2	f_3
1	0 V	18.0 GHz	> 30 GHz	> 30 GHz
2	18 V	9.4 GHz	> 30 GHz	> 30 GHz
3	28 V	5.7 GHz	17.5 GHz	> 30 GHz
4	38 V	2.4 GHz	9.0 GHz	14.3 GHz

The measured normalized patterns are shown in Figure 5. Some ripple can be noticed in State 1 of the antenna due to mismatch from the coaxial SMA connector. The measured patterns agree well with the simulated ones. The measured radiation pattern for the xz-plane ($\varphi=0^o$) is not presented as before since it shows an omni-directional pattern in that plane.

This work presents the possibility of adding an additional level of reconfigurability to a device or system by simply integrating RF MEMS switches with different geometries. A sequentially-reconfigurable RF MEMS multiband antenna was designed, fabricated and tested on a flexible, organic substrate for the first time. The purpose of this research was not only to illustrate a method of biasing MEMS-reconfigurable antennas without the need for DC bias lines, but also to illustrate how the antenna performance can be enhanced by increasing the number of resonant frequencies. The final device does not have any additional lines to bias the switches, while the antenna exhibited four principle resonant frequencies with good radiation characteristics. By using MEMS switches, the losses are kept to a minimum. Three different switch geometries were integrated into a Sierpinski antenna with different actuation voltages. The simulated and measured response agreed well. This technology can be applied to many other devices, including tuners, tunable filters, other antenna geometries, or signal splitters.

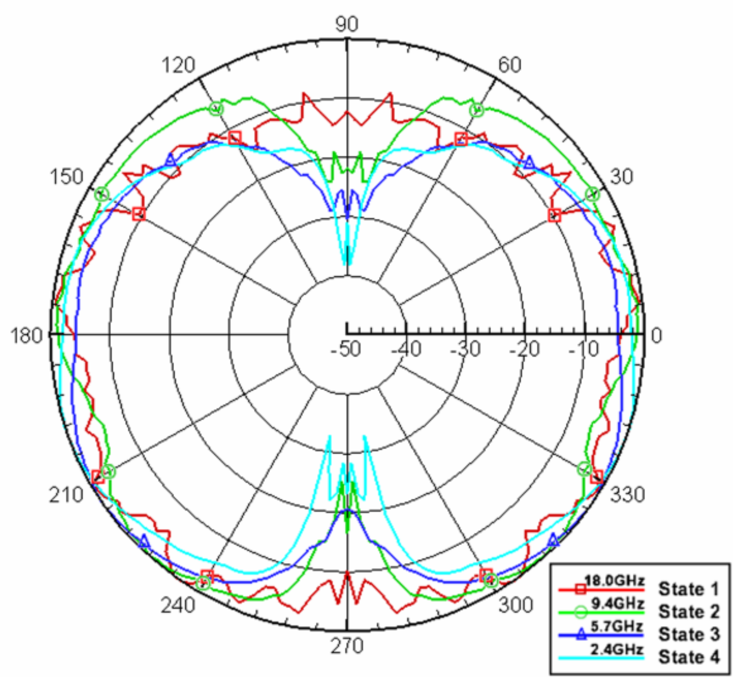

Fig. 5. Measured radiation pattern for φ=90^{o} (zy-plane) for all four states of the designed Reconfigurable antenna at the first resonant frequency. Broadside radiation with similar patterns at each frequency is achieved. The different curves at 2.4GHz, 5.7GHz, 9.4GHz, and 18.0GHz validate the multiband characteristics that can be achieved by using MEMS to reconfigure such antenna designs.

2. Pattern Reconfigurable Antenna on Organic Substrate

During the reporting period we collaborated with UIUC on the development of a pattern reconfigurable antenna on LCP with MEMS switches. The antenna design was preformed by UIUC and more details are given in their report. Fig. 6 shows a set of nine reconfigurable antennas.

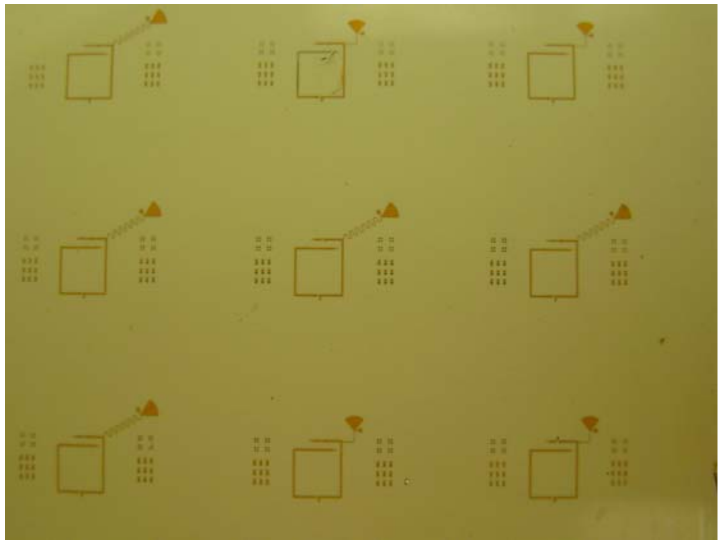

Fig. 6 Photo of fabricated pattern reconfigurable antennas on LCP.

In order to achieve reconfiguration ohmic MEMS switches, similar to the ones used for the Sierpinski antennas, were integrated on the LCP substrate. Fabrication of this antenna, however, was more challenging as vias going through the substrate had to be manufactured. Via technology is typically not compatible with MEMS switch technology and extra caution had to be taken. Measured results from this antenna will be reported by UIUC.

In order to develop planar antennas at lower operating frequencies per Army's requirements, we also manufactured a stacked patch antenna with integrated MEMS switches. We have modified the design of Ruyle and Bernhard to incorporate MEMS switches to achieve reconfigurability. A schematic of the design with Single Pole Single Throw MEMS switches is depicted in Figure 7a-7b. Duroid materials 5880 ($\varepsilon r1 = 2.2$) and 6002 ($\varepsilon r2 = 2.94$) have been procured. Since these materials are 3.175 mm thick, several test runs were needed for optimization of through hole laser drilling. This task was time consuming as the substrate was thicker due to the lower operating frequency of the antenna. Figures 7c-7d show the geometry of the drilled holes through the laminated 18 micron copper on one side. Figure 8 shows the final organic layer stack-up. A procedure for the integrated fabrication of MEMS switches was also developed. Fig. 9 shows the final dimensions of the fabricated patch antenna with RF MEMS switches. The final dimensions including the bias lines are 51 mm by 50.5 mm. Fig. 10 shows a view of a single RF MEMS switch. The varying color on the bias lines are from the varying thickness of the nitride layer on the CrSi. The nitride layer is partially etched in the subsequent steps of the nitride deposition step, but it is sufficiently thick to protect the CrSi layer and not be etched completely. Fig. 11 shows a closer view of the RF MEMS switch, and from the focus of the image, it is clear that the membrane is not stuck to the bottom. The individual MEMS switches actuated at 80 – 90 Volts. Antenna measurements will be reported by UIUC.

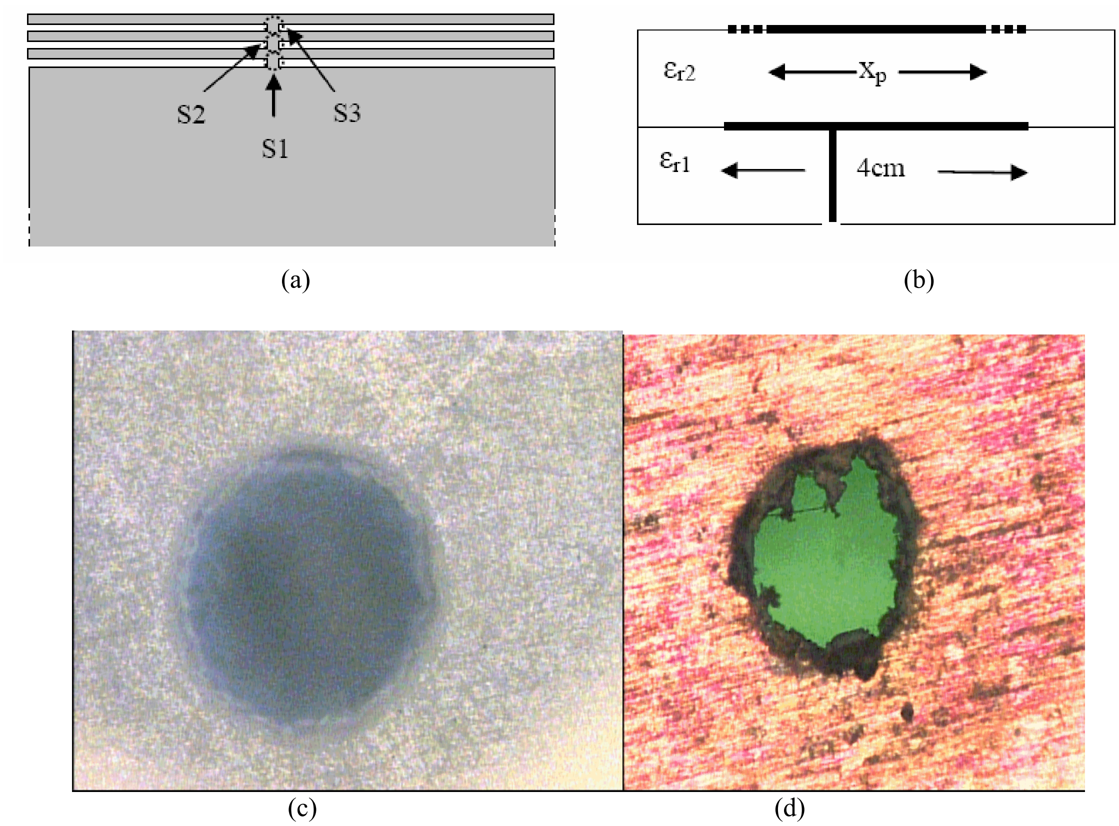

Fig. 7. Reconfigurable antennas with (a) top and (b) side views (S1, S2, and S3 are the MEMS switches); (c) Laser drilled through hole in Duroid 5880 material. Substrate thickness 3.175 mm, hole diameter at the entrance 1.35 mm (c) and at the exit 1.05 mm (d).

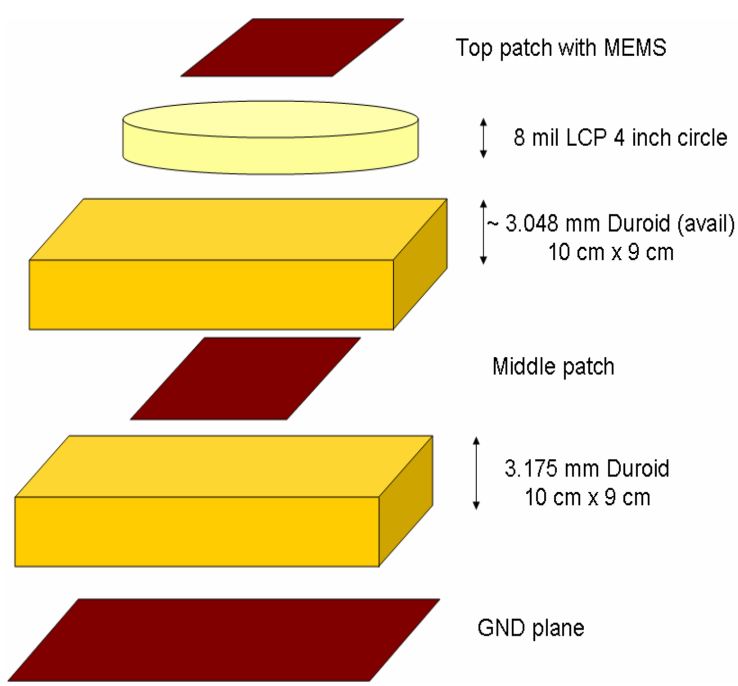

Fig. 8 Stack up of the reconfigurable patch antenna.

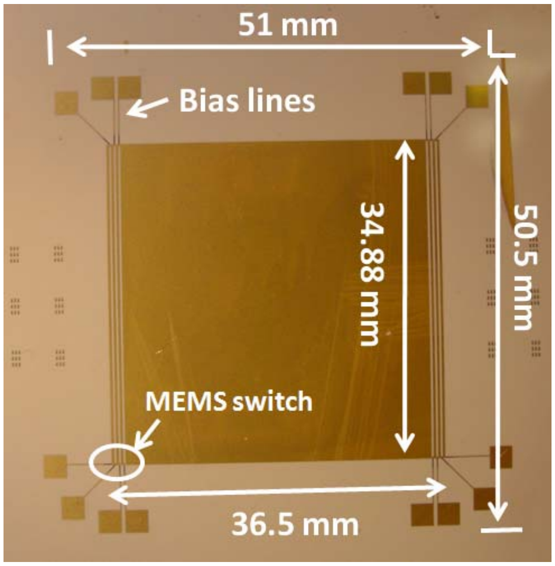

Fig. 9: Fabricated patch antenna with RF MEMS switches.

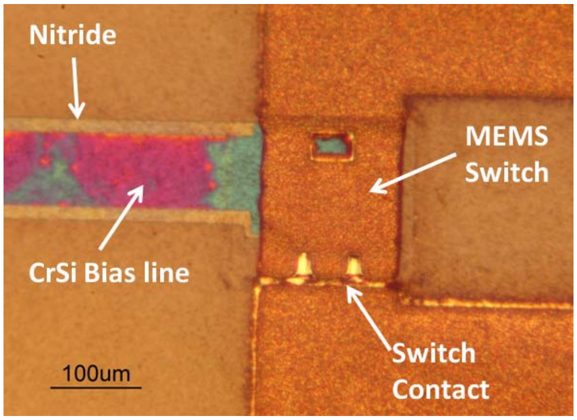

Fig.10: View a a single ohmic contact MEMS switch.

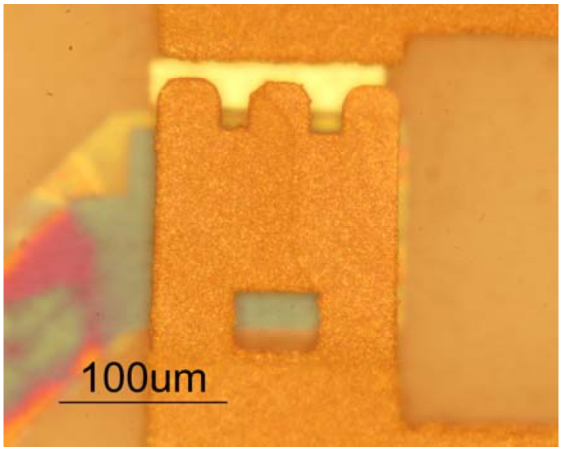

Fig. 11: Close up view of the RF MEMS switch.

3. Localized Packaging of RF MEMS Switches on Organic Layers

3.1 Introduction

During the reporting period a low cost localized heating packaging method on liquid crystal polymer (LCP) for temperature sensitive devices such as the capacitive RF MEMS switch was developed. Simulations of the heating element structures were performed to examine the thermal characteristics of the bonded regions and switch. Heating lines were fabricated on LCP using the copper cladding, requiring only one photolithography and etch step. The MEMS cavity was formed with two 1 mil layers of low-temp LCP that were etched with a CO2 laser system. The layers were bonded with localized-heating by passing 7 A of *DC* current through the heating element while compressing the 4 layers together. The bonded switch was submerged in 60◦C water for 24 hours to test seal quality.

This work investigates the use of patterned lines on copper clad LCP as a low-cost method for packaging RF MEMS switches (Fig. 12). A significant advantage of this method is the use of heating lines external to the stack-up allowing for easy removal and hence no impact on RF performance as seen in previous work. Heating lines are fabricated on LCP requiring only one photolithography and etch step, and the MEMS cavity is formed with two 1 mil layers of low temp LCP that are etched with a CO_2 laser system.

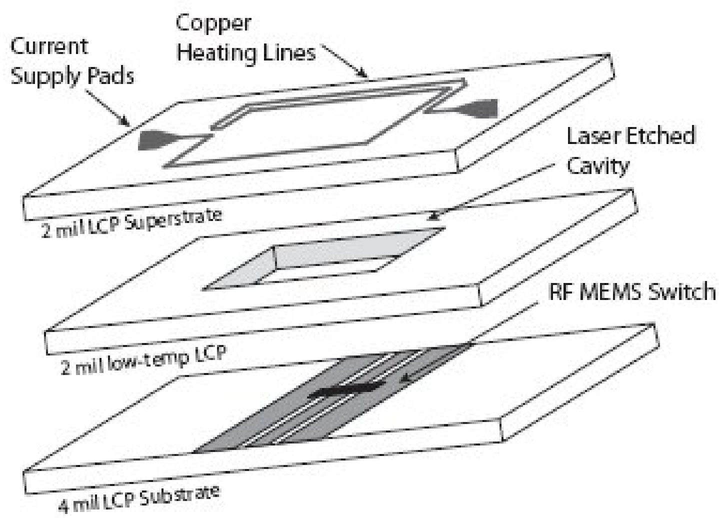

Fig. 12. Layer stack-up for localized heating method.

3.2 Implementation

A capacitive membrane MEMS switch was fabricated on a 4 mil LCP. Fig. 13 shows the fabricated switch, featuring meandered springs to reduce pull-down voltage. The heating element was fabricated on copper clad 2 mil LCP. 500 μm wide lines were patterned via photolithography and etched in copper etchant. The lines form a rectangular region that encircle the desired bonding area, consisting of 3- 4 heating lines per side to facilitate a wider bonding region. The heating lines were tapered out to a large 1 inch wide line at either end. The large lines provide higher conductivity which generates significantly less heat than the 500 μm lines during bonding and allows easy access for the bonder current supply. Tapers limit excessive heating at the junctions between line widths resulting from high local resistance.

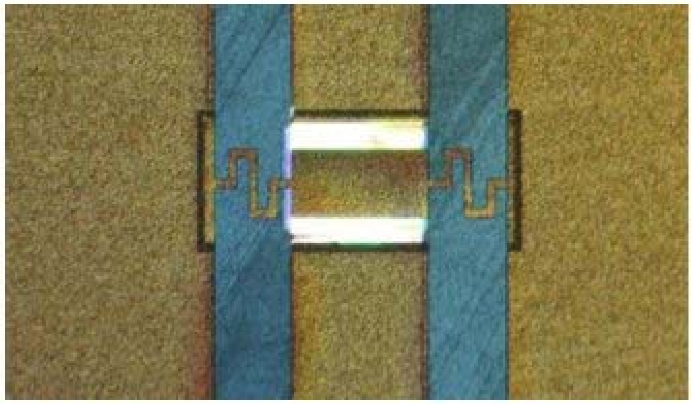

Fig. 13 Capacitive membrane MEMS switch used in the bonding process.

A cavity for the MEMS switch was fabricated from two pieces of 1 mil low-temp LCP. These layers were etched with a CO_2 laser system to provide room for the switch and contact the area of the heating rectangle on the heating element sample. The four layers were sandwiched together and pressed between high-temperature glass slides with enough pressure to keep the heating elements from delaminating during heating. Glass was used as it is a poor thermal conductor, which keeps heat generated at the heat elements from sinking to the slides and reducing heat flow to the internal LCP layers. 7 A of *DC* current was applied to the heating element, pulsed at 60 Hz for 30 seconds. Switching the current allows for better thermal transfer vertically through the layers without causing the top layer to heat excessively. Higher currents can be used for faster bond times, but this causes the heat on the top layer to potentially damage the top LCP or copper lines. The patterned heating elements reside on the topside of the heating layer, so they can be easily etched after bonding. This requires thermal transfer through the top layer, but removes impact of the copper heating lines on RF performance. The bonding method can easily be scaled up to accommodate multiple individually packaged devices (wafer-scale packaging). Wider lines can be used between bonding regions to limit the areas where the melting temperature is reached. Expanding the bonding area or bonding additional regions simultaneously requires the same amount of current (assuming a constant heating line width is kept at the bonding regions), but higher voltage resulting from the larger resistance seen at the current supply terminals. Using thinner metal layers will result in higher resistance for the same line geometry, trading current requirements for higher voltages. Because the heating lines are patterned, complicated seal shapes and extremely varied seal sizes and geometries can be created for simultaneous bonding at wafer-scale. A photo of the assembly elements is shown in Fig. 14.

3.3. Measurements

The switch was measured from 2-40 *GHz* on an Agilent 8510C network analyzer with an SOLT calibration. Measurements of the switch were taken before any bonding operations took place. After bonding, the switch was submerged in 60◦C water for 24 hours. After removal, the package was peeled apart without any interruption to the internal state of the cavity (ie, no heating to remove residual moisture), and the switch was measured a second time. Before and after measurements can be seen for the down (actuated) state and the up (non-actuated) state in Figs 15 and 16 respectively. The switch exhibits 0.5–0.6 *dB* loss in the up state, which includes 1 cm of line loss for the CPW line. Removing line loss, the switch generates a loss of 0.2–0.3 *dB* up to 40 *GHz*. Return loss in the up state is better than 20 *dB* for 2-40 *GHz*. In the down state, the switch maintains isolation better than 20 *dB* for frequencies > 15 *GHz*. The switch was designed with a high frequency resonance to provide the highest level of RF performance at frequencies where active switches (pin diodes, FET technologies, etc) are unable to match the capability of the capacitive membrane MEMS switch. No appreciable difference in RF performance was observed in before and after measurements, indicating that no water was introduced to the internal packaged cavity during water submersion.

To test the impact of the bonding method on RF performance, an FGC line was measured before and after bonding. The after measurements were taken with the heating lines removed post-bonding, leaving the seal intact. Fig. 17 shows very little difference between these two cases, showing the RF impact of the sealing method is negligible.

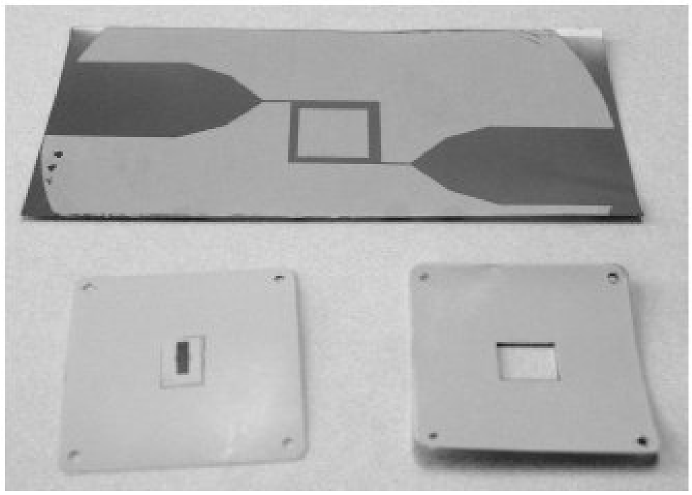

Fig. 14 Photograph of heating element superstrate, laser etched spacer layers and MEMS LCP substrate prior to bonding.

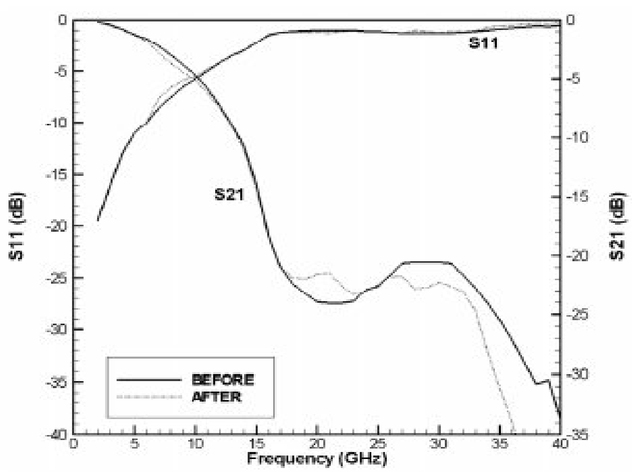

Fig. 15 Measurement results of switch before and after water testing in DOWN (actuated) state

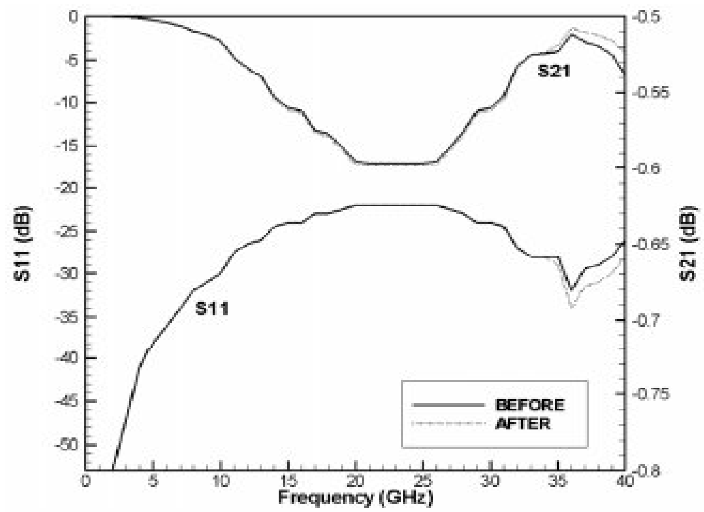

Fig. 16 Measurement results of switch before and after water testing in UP (non-actuated) state.

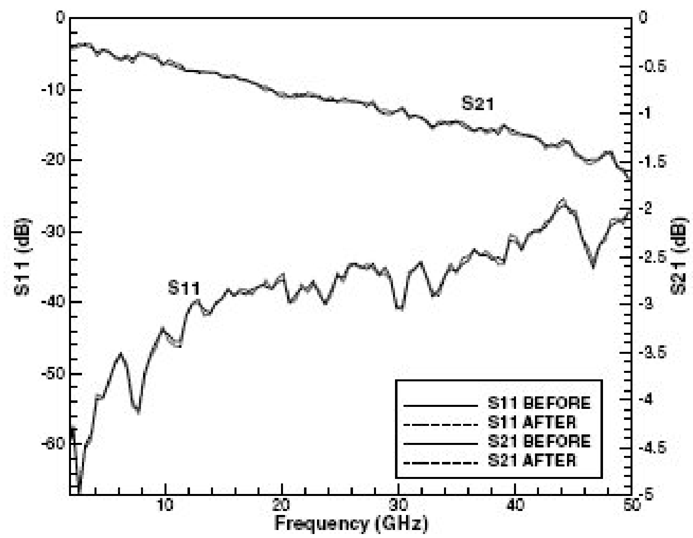

Fig. 17 Measurement results of FGC line before and after bonding with heating lines removed.

3.4 Moisture Lifetime Testing of RF MEMS Switches Packaged in Liquid Crystal Polymer

In this work, MEMS switches were packaged in a polymer material and subjected to two humidity conditions. The polymer material chosen was liquid crystal polymer (LCP). LCP has been well-documented as a low-cost material that is also low-loss up to 110 GHz. According to the manufacturer, LCP has a "water absorption" of 0.04%. S-parameter results are shown before and after testing to determine the effects of the moisture exposure. The lifetime of an LCP packaged switch was extrapolated for jungle, ambient, and desert-like conditions.

The MEMS switches used in this work were fabricated directly on the LCP material. Single-supported, capacitive-type switches were used although the experimentation and results are applicable for ohmic and double-supported switches as well. These switches were designed to work at 30 V actuation. They are made with 1 um plated gold suspended approximately 1 um above the substrate. The overall dimensions of the membrane are 200 um 400 um. The fabricated MEMS switch is shown in Fig. 18. Since the MEMS switches will be contained in a package entirely made of LCP, there are two possible sources of moisture: through the LCP material and through the seal. Ideally, MEMS switches would be packaged between layers of LCP using wafer-scale (or global) thermocompression bonding. However, LCP melts at 290 ^{o}C and MEMS switches experience plastic deformation above 200 ^{o}C. Therefore, it is necessary to implement the bonding process using an epoxy or a localized heating technique.

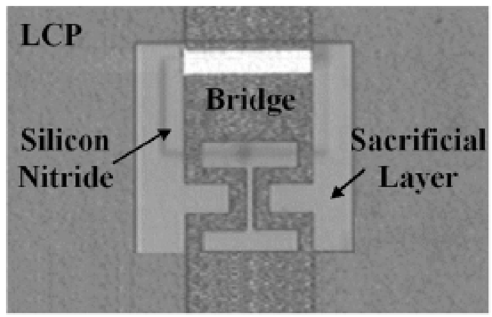

Fig. 18. Photo of fabricated MEMS switch on LCP. The sacrificial layer is removed to facilitate the suspended bridge.

Since the objective of this research is to determine the moisture resistance of LCP alone, no epoxy bonding was used. Instead, three sample configurations were investigated:

1) Global lamination with an air-filled cavity (no MEMS switch).

2) Global lamination with an air-filled cavity and 18 um thick copper on the top and bottom (no MEMS switch).

3) Localized ring bond with an air-filled cavity and MEMS switch.

These configurations are shown in Fig. 19. For Configurations 1 and 2, global thermocompression bonding was performed. For this bonding, the layers are heated to the melting temperature over the course of 10 min. They are then held under compression for 45 min. The sample is continually held under compression until it cools to room temperature. Since this process is slow, the molecules have time to arrange in the same crystal-like state as they did before melting. Even though RF MEMS switches can not survive this process, it does represent the best-case scenario that can be achieved with direct LCP to LCP bonding. Bond widths of 2, 5, and 10 mm were tested. For Configuration 3, a seal around the MEMS switch was formed using resistive heating of thin copper lines. The layers of LCP are heated under force to the molten state in less than 5 s. They are then held in place at this temperature and pressure for 30 s to ensure that uniform melting has occurred.

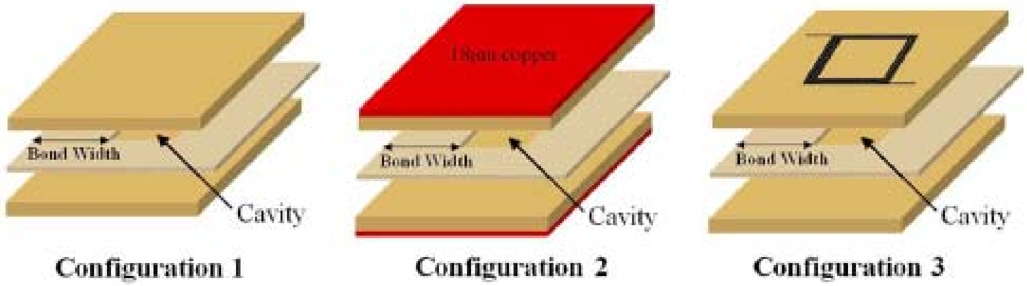

Fig. 19. Three sample configurations. A cavity is formed by bonding two layers of high-melt LCP to a layer of low-melt LCP with a hole cut in the material. The bond width dimension is shown.

While maintaining a constant pressure, the temperature is allowed to cool down to room temperature over the course of 5 min. Since the entire process is quick, the heat from the bonded areas does not affect the MEMS switches. The bond width is approximately 2 mm. To provide the best possible bond quality and consistency across samples, several precautions were taken. First, all of the samples were plasma cleaned prior to bonding to remove any trace amounts of dust, dirt, oils, or other impurities. Second, all processing was performed in a class 10 cleanroom environment. Third, all cavities are of the same size (2cm x 2cm x 50μm or 0.02 cm^3). Finally, all samples were processed at the same time in a low-humidity environment.

Before and after testing, all samples were baked for 1 h at 100 ^oC on a hot plate. This step is necessary to remove any surface moisture that will not compromise the integrity of the package but can skew the weight measurements. Precautions were taken to protect the samples from dirt and oils. All weight measurements were repeated a week after sitting in ambient conditions with identical results. It can be concluded that this dry bake temperature and duration were sufficient. All measurements were taken with a scale that has five digits of precision and is enclosed to eliminate the effects of room pressure changes. According to Military Standard 883 G, Method 1014.12, a cavity with a volume of 0.02 cm can pass the seal leak test with less than 2 mg of weight gain.

To evaluate long duration exposures to the elements (up to 10 years), a test was performed at 100 ^oC and 100% relative humidity for 1, 5, and 10 h. The measured weight gain from this test is shown in Table II. A visual inspection of the MEMS in Configuration 3 showed that the switches had been affected by moisture. Measurement results confirmed that the switches did not survive the test and were stuck in the DOWN state. In this work, only the 2 mm bond width was tested for Configuration 3. This is due to the difficulty in realizing wide bond widths using localized heating techniques. The 10 h test was not completed for this configuration since the 1 and 5 h samples leaked profusely. There are two samples that gained a great deal more moisture weight than the others (Configuration 1, 10 mm, 10 h and Configuration 2, 10 mm, 1 h). A visual inspection did not find any indication of why these samples leaked profusely. Since LCP is a polymer, defects in the material are always possible and can not be avoided.

TABLE II

WEIGHT GAIN MEASURED FOR THE THREE CONFIGURATIONS AT 100 C AND 100% RELATIVE HUMIDITY. AT THIS TEMPERATURE AND HUMIDITY, 1 H OF TESTING IS EQUIVALENT OF ONE YEAR IN AMBIENT CONDITIONS

Bond Width/Duration	Config. 1	Config. 2	Config. 3
2mm/1 hour	0.3mg	0.1mg	5.5mg
2mm/5 hour	0.3mg	0.5mg	8.2mg
2mm/10 hour	0.8mg	0.2mg	Not tested
5mm/1 hour	0.4mg	0.7mg	Not tested
5mm/5 hour	0.5mg	0.2mg	Not tested
5mm/10 hour	0.4mg	0.1mg	Not tested
10mm/1 hour	0.5mg	1.5mg	Not tested
10mm/5 hour	0.6mg	0.3mg	Not tested
10mm/10 hour	6.4mg	0.3mg	Not tested

To evaluate the short term effects of moisture, a second test was performed at 85 ^{o}C and 85% relative humidity. This test has roughly one-fifth the acceleration factor of the 100 ^{o}C/100% test and is the equivalent of about three months of ambient exposure. The weight gain from this test is shown in Table III. All tests passed the Military Standard. The post-test S-parameter measurement results are shown in Fig. 20. The 30 min switch was able to actuate without problems at 30 V [Fig. 20(a)]. The 50 min switch had deformed enough that it was only able to move a fraction of a micron at 100 V. Only a slight change in the response was measured [Fig. 20(b)]. The 70 min switch was unable to move at all [Fig. 20(c)]. Since the 30 min switch survived the moisture exposure, a comparison can be made in the S-parameter measurements before and after testing. These results are shown in Fig. 21. This comparison confirms that there was no degradation in the performance due to the moisture exposure.

TABLE III

WEIGHT GAIN MEASURED UNDER 85 C AND 85% RELATIVE HUMIDITY CONDITIONS. ALL SAMPLES HAVE A 2 MM BOND WIDTH

Sample	Weight Gain	Switch worked after testing?
Config. 1 - 30 minutes	0.1mg	N/A
Config. 1 - 50 minutes	0.1mg	N/A
Config. 1 - 70 minutes	0.1mg	N/A
Config. 3 - 30 minutes	0.1mg	YES
Config. 3 - 50 minutes	0.2mg	NO
Config. 3 - 70 minutes	0.2mg	NO

From the data in Table II, several conclusions can be made:

1) All packaged cavities resulted in at least 0.1 mg of weight gained.
2) The presence of the 18 um thick copper had very little effect (less than 10% improvement) on the amount of weight gained. This suggests that most of the leakage is through the seal, not the material.
3) Most of the weight gain occurs within the first hour of testing.
4) The bond width has a negligible effect on the rate or amount of weight gained

5) For some cases, as the duration is increased, the weight gain decreases. This demonstrates the inconsistency with polymer materials.
6) Of the 18 globally laminated samples in Configurations 1 and 2, only one test failed the Military Standard. Both locally bonded samples in Configuration 3 failed.

The data in Table III supports these conclusions as well. This work has also shown that passing the Military Standard for seal quality does not guarantee that the package is suitable for MEMS switches. All of the cases shown in Table III passed the standard but only one switch actually survived. If 0.1 mg of weight gain is the actual amount of moisture that the switch can tolerate for this cavity size, then the data in Table II suggests that even the best-case bonding effort is not suitable for reliable MEMS packaging. Sixteen of the eighteen samples gained more than 0.1 mg of moisture weight.

Aside from measurement data, a visual analysis can also provide an indication of the damage that has occurred from moisture exposure. The metal bridge membrane is relatively unaffected by low levels of moisture. As the humidity level within a cavity is increased, the edges of the membrane begin to curl. Effectively, this strengthens the bridge in the axis of motion. This type of curling was seen in the switches exposed to the 85 ^{o}C/85% condition for 50 and 70 min. This is why the membrane did not actuate even at very high voltages. The curling was less severe in the 50 min sample which is why it was able to deflect slightly. Both of these samples were stuck in the UP state. As the humidity level increases further, moisture begins to collect on the metal membrane and the signal line beneath it. If the humidity level increases high enough, the surface tension in this moisture will pull the switch down. This effect was seen in the switches exposed to the 100 ^{o}C/100% condition. These switches were stuck in the DOWN state. Using the acceleration factors, it can be extrapolated that an LCP packaged

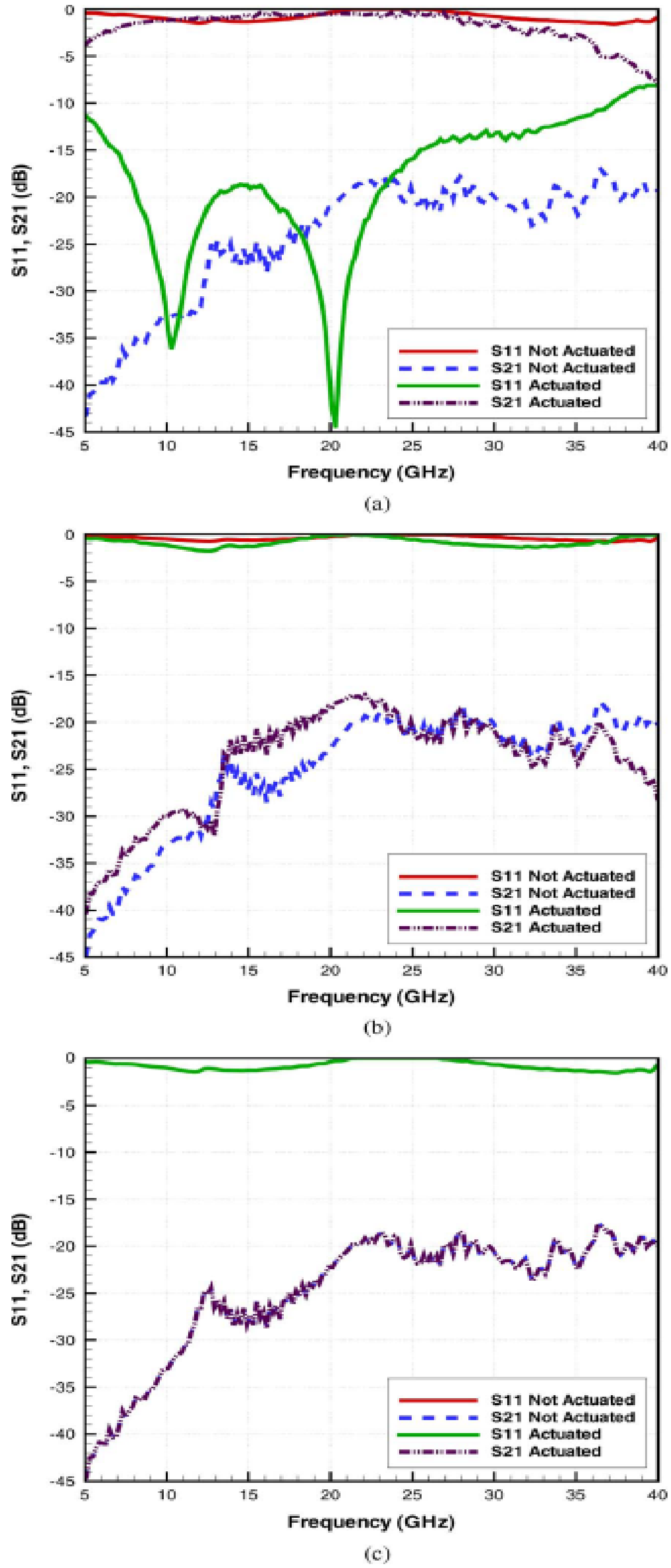

Fig. 20. S_{11} and S_{21} measurement results for the three 85 C/85% moisture test durations. Measurement 4(a) shows a working switch with a 30 V actuation. Measurement 4(b) shows a non-working switch with some movement at 100 V. Measurement 4(c) shows a switch stuck in the not actuated (UP) state.

MEMS switch using localized ring bonding (Configuration 3) should survive 7–10 h in jungle conditions, 5–7 weeks in ambient conditions, or 1.4–1.8 years in desert conditions. It is possible that other bonding methods and process conditions may be able to improve the moisture resistance and extend these durations.

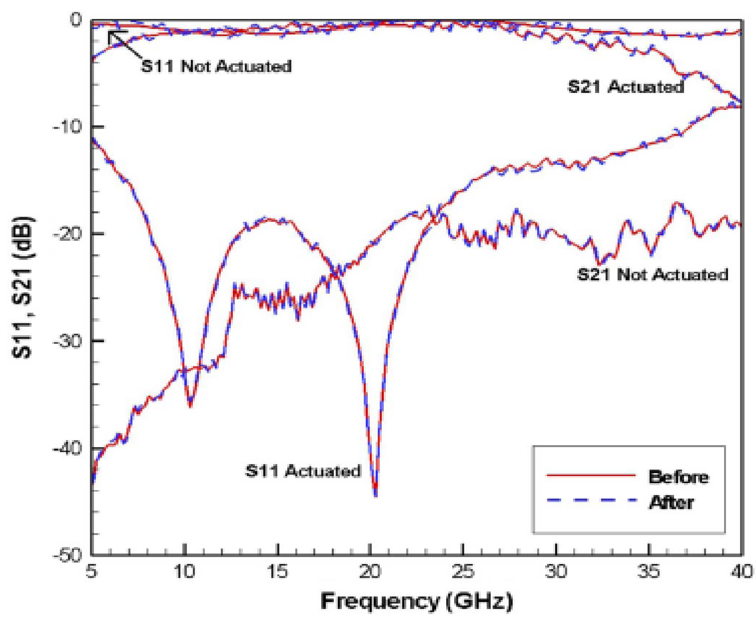

Fig. 21. S-parameter measurement results are shown for the working 30 min switch before and after moisture exposure. Less than 0.1 dB and 0.5 dB difference were measured between the S_{21} and S_{11} results, respectively. This is within the tolerance for measurement error.

4. Design of PZT MEMS Switches and Circuits

4.1 Introduction

During the reporting period graduate student David Chung completed a summer internship at the ARL MEMS group in Adelphi, MD. David's internship focused on the design and optimization of a SP4T (Single Pole Four Throw) switch and a two bit phase shifter with an operating frequency of 30 GHz using the SP4T. The design is unique in that it uses a piezoelectric MEMS (Micro-Electro-Mechanical Systems) switch as the foundation for these designs. The piezoelectric switch has lower actuation voltage (below 10 V) compared to other electrostatic MEMS switches. The switch in this design is an ohmic contact series switch using lead zirconate titanate (PZT) thin film actuators. The SP4T exhibits an isolation less than 20 dB along with less than 1 dB of insertion loss from DC up to 40 GHz. In addition, it is possible to design the SP4T switch for even higher frequencies. Using two cascaded SP4T designs, a two bit phase shifter has been designed with different path lengths. The averages loss is less than 1.6 dB at 30 GHz while maintaining an isolation below 20 dB on high resistivitiy silicon substrates. This result is from simulations with ADS including substrate and conductor loss but excluding the actual loss from the PZT MEMS switches.

4.2. Single Pole Four Throw (SP4T) Design

The simulation tools used were ADS Momentum (2.5-D MoM [Method of Moments] solver), HFSS (3-D FEM [Finite Element Method] solver), and AutoCad for design and file conversion. As shown in Fig. 22, multiple designs were considered for the optimum case of a Co-Planar Waveguide (CPW) configuration SP4T.

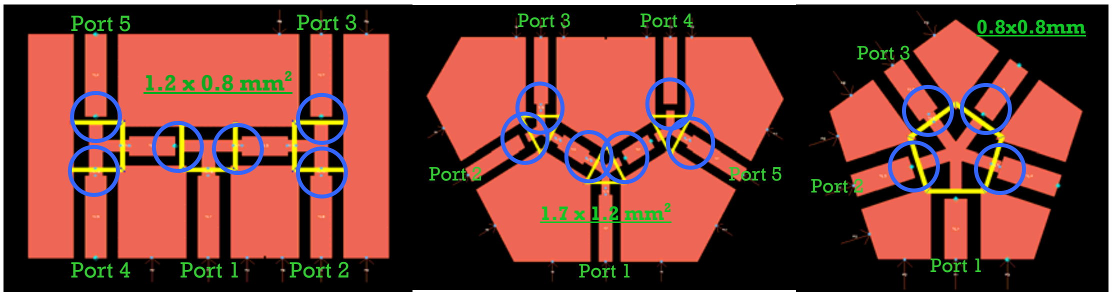

(a) (b) (c)

Fig. 22 Various designs of SP4T noting the location of the MEMS switches with blue circles.
(a) 90 degree bends for a dimension of 1.2x0.8mm^2 (b) 120 degree bends at 1.7x1.2 mm^2
(c) Pentagon shape junction at 0.8x0.8 mm^2.

The brown colored part is the bottom metallization (0.8 μm Ti/Au) and the yellow parts are the air bridges connecting the ground planes all using gold (2μm Au). The air bridges are essential at any discontinuity as they suppress any higher order modes that can arise. At the edges of these yellow air bridges, there are gold anchors connecting the air bridges to the ground plane that can not be seen in the picture because of the small size. The main parameter of interest is the width of each junction as it governs how well the characteristic impedance is matched to the input and output, designed to be 50. Comparing the three different designs, the important point is to see that the pentagon shape is the smallest and shortest route for a signal going through a SP4T, but there are tradeoffs that will be discussed in the next section. In this simulation, due to the memory requirement for complex designs, the actual MEMS switches have not been modeled. The off state is noted as an open part in the circuit and the on state is assumed to be a connection of metal. Referring to Fig. 24, it can be seen that the PZT switch is well modeled be a series C in the off state and a series R (~1.5 Ω) in the on state, thus justifying this simplification. However, the following simulations have assumed a more ideal case to simplify the optimization process. The area for the MEMS switches are on the outer parts of the air bridges where the blue circles are marked. The input, leading into the junction from port 1, does not need a switch since it will always be the input for the signal. For example, there will be six switches in Fig. 22(a) and Fig. 22(b), and four switches in Fig. 22(c). Thus, another advantage of the pentagon shaped junction is that it needs fewer switches for operation and the signal will only go through one switch for these junctions leading to smaller loss. Similar designs for the SP4T junction have been developed, but they are only useful for operating frequencies below 20 GHz. Using piezoelectric MEMS switches, the limitation goes far beyond 20GHz while the isolation is greater than 20 dB even at higher frequencies.

4.3 Two Bit Phase Shifter Design

The two bit phase shifter was created by cascading two SP4T junctions. The phase states of 0°, 90°, 180°, and 270° are achieved by choosing different path lengths that correspond to each state. The overall design is shown in Fig. 23(a). The overall dimension is 2.6mm by 1.9mm and again the bends are crowded with air bridges to suppress undesired modes. It is essential to simulate each of the bends to optimize the responses as they introduce approximately 0.1 dB of loss and the air bridges can add parasitic capacitances.

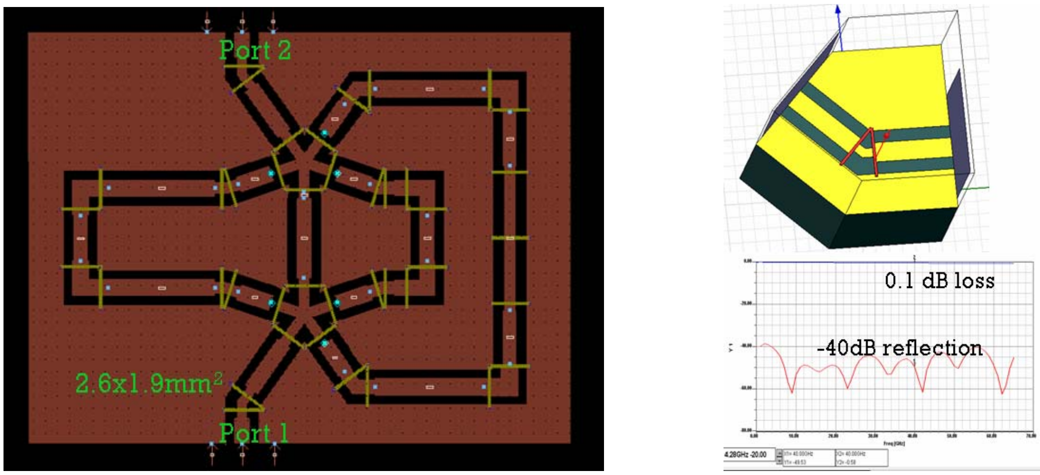

(a) (b)

Fig. 23 (a) The design of a 2 bit phase shifter with overall dimension of 2.6x1.9mm^2
(b) The HFSS model of a 136° bend and its simulated response.

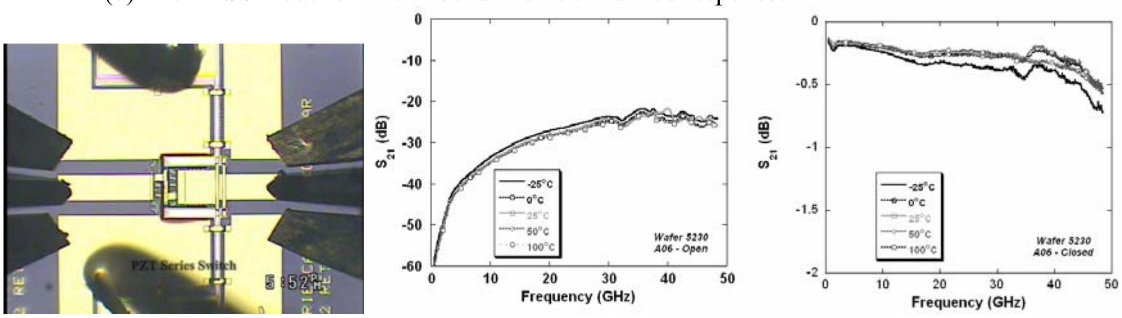

(a) (b) (c)

Fig. 24 (a) Image of fabricated piezo-electric MEMS switch (b) Isolation of MEMS switch in off state
(c) Insertion loss of switch in on state [4].

Therefore, as in Fig. 23(b), a model of a 136° bend was simulated in HFSS. The result is approximately 0.1 dB of loss and -40 dB of reflection at 30 GHz showing that it is well matched. Likewise, 90°, 108°, 126°, 144°, and 162° bends have been optimized to give similar responses. The dimensions of the line segments and bends have been modified to best match the input and output as well as the desired phase.

4.4 MEMS switch response

The piezoelectrically actuated MEMS switches has been designed, fabricated, and measured in the ARL. Fig. 24 shows an image and measured response of the switches. In the off state (Fig. 24(b)), the measured isolation is better than 20 dB even for frequencies greater than 40 GHz. The measured insertion loss (Fig. 24(c)) at 30 GHz is 0.33 dB and 0.41 at 40 GHz. In addition, the median actuation voltage has been reported as 3.9 V with ±1.07 V with less than 750 pW of power consumption. These MEMS switches show promising attributes and are very attractive for phased array applications.

The simulation results are shown in Fig. 25, where (a) is the 90° design, (b) is the 120° design, and (c) is the pentagon shape response. Since the structures are symmetric, only S_{21} and S_{31}

have been shown. The 90° design exhibits 0.5 dB loss because there is a small resonance at 30 GHz. Compared to the other two designs, the 90° design is not as efficient in its size or response compared to the other two designs, so it has not gone through an optimization to eliminate the resonance that is from the structure. However, other than the resonance, the overall performance is good past 50 GHz as the isolation is better than 20 dB. The 120° design shows 0.3 dB loss at 30 GHz. Again, the design is well matched and the isolation is less than 20 dB up to 60 GHz illustrating that higher frequency designs are possible. The pentagon design exhibits 0.25 dB loss at 30 GHz.

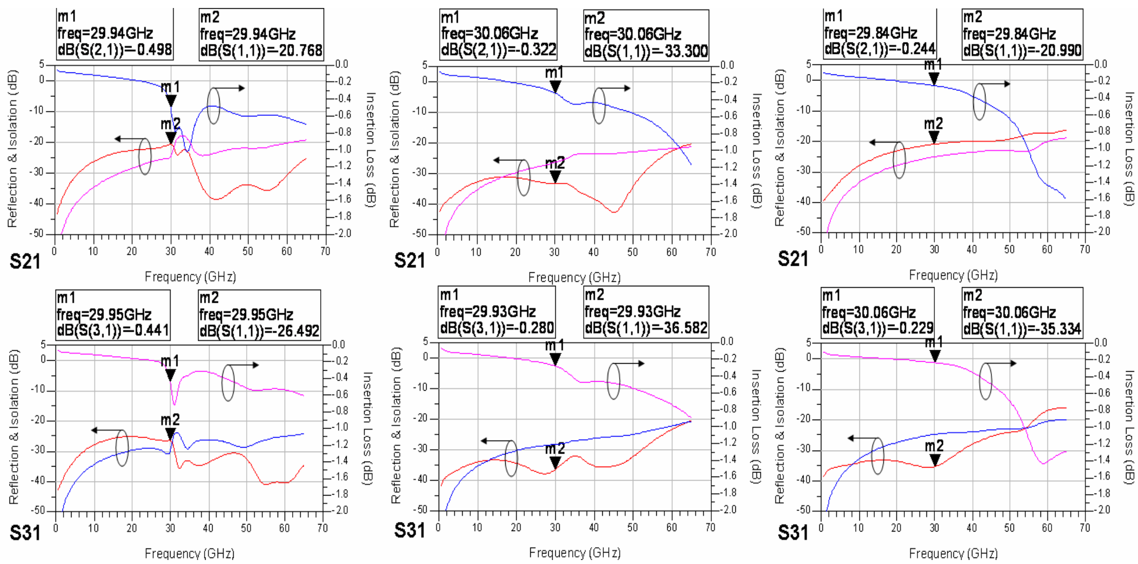

(a) (b) (c)

Fig. 25 Simulated response of (a) 90° (b) 120° (c) Pentagon SP4T responses

The reflection (S_{11}) becomes significant, greater than -20 dB, for the S_{21} response around 40 GHz as there is a sharp turn that the signal needs to pass as seen in Fig. 24(c).

The optimal junction width for the pentagon shape is 40 µm for the ADS momentum model and 27 µm for the HFSS model. Because HFSS is a three dimensional solver and ADS momentum is 2.5 dimensions, HFSS appears to provide a more feasible solution. Nevertheless, ADS momentum has been used for the subsequent simulations because it is more user-friendly and requires less memory.

These simulations did not include the substrate loss which seems to add about 0.1 dB to the results. For the phase shifter design, the pentagon design SP4T is best fit as it has smallest footprint and has the least loss. However, for operating at higher frequencies, the 120° design seems more suitable.

4.5. Phase shifter simulation results

As shown in section 4.3, two SP4T were cascaded with a delay line to create a two bit phase shifter. Looking at Fig. 23(a), the shortest path is the 0° state which corresponds to Fig. 26 (a). The 90° state is Fig. 26(b), 180° state (c), and 270° state (d). The phase shifter has been optimized at 30 GHz at which a resonance lies. The source of this resonance is still being investigated. These simulations have incorporated both the conductor and substrate loss. The conductor loss starts to dominate as the paths get longer and longer, but there is no way to avoid such loss. On average, the loss is 1.6 dB which corresponds to 0.8 dB/bit. The loss is the summation of the conductor loss, substrate loss, the bends, and the SP4T junctions. The conductor and substrate loss has been measured to ~0.25 dB/mm, the bends add ~0.1 dB/bend, and finally the junctions would add ~0.3 dB/junction. The 0° state is approximately 1mm long and each of the next states is about 1mm longer than the previous shorter state. The expected average loss including the MEMS switches is approximately 2 dB.

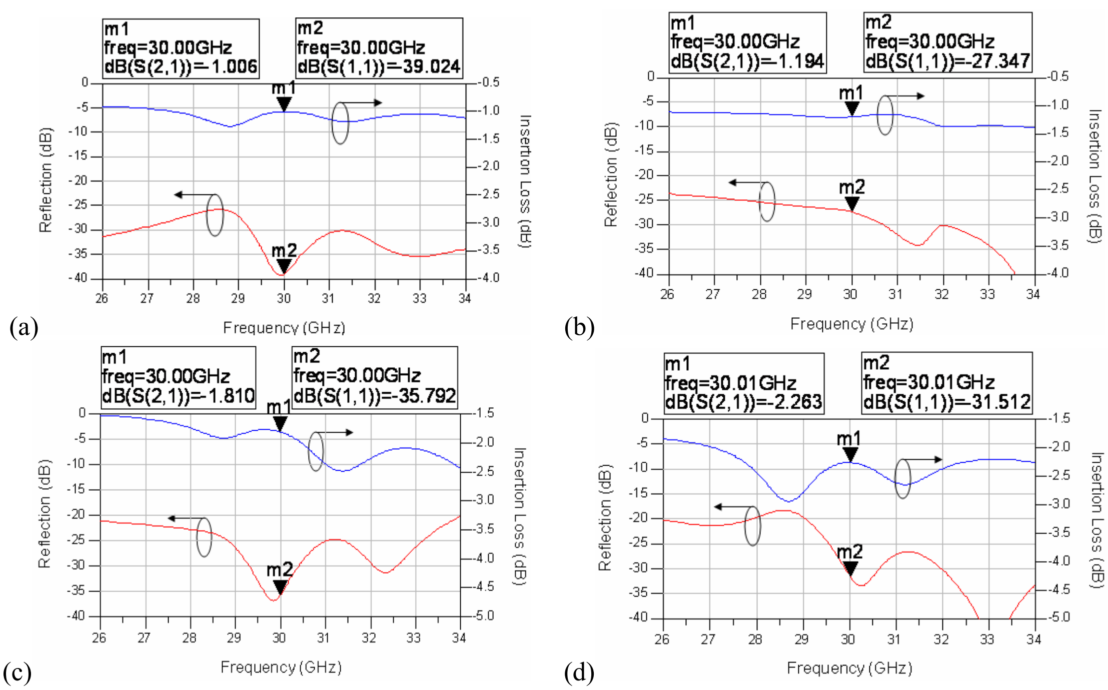

Fig. 26 S-parameter of the phase shifter in different states (a) 0° shortest (b) 90° (c) 180° (d) 270°.

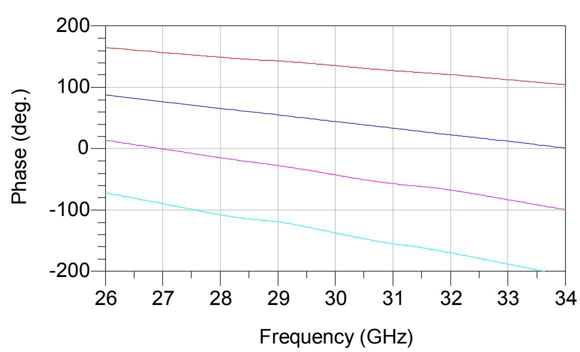

Phase	Value(°)	Error(°)
0°	135.36	NA
90°	44.62	0.74
180°	-42.88	-1.76
270°	-137.85	3.21

Fig. 27 Simulated phase diagram.

Table IV Phase values and error.

The simulated phase values are shown in Fig. 27 and Table IV. Since the 90° phase difference only needs to be relative to each other, the shortest path or 0° has been used as the reference. The error is less than 3° on average and shows good agreement with the expected value.

Photos of the fabricated switches are shown in Fig. 28. The measurement of the s-parameters was carried out using an Agilent E8361A vector network analyzer from DC to 50 GHz. The SP2T in Fig. 28(a) has one input and two PZT MEMS switches leading to the outputs. The SP4T has one input and four PZT MEMS switches leading to outputs. In both cases, any given path will require one PZT MEMS switch to operate. The difference between Fig. 28(b) and Fig. 28(c) is that (b) does not have an undercut in the spoke region and has a spoke width of 27 µm. The spoke region in (c), marked with a circle and arrow, has the silicon removed beneath it and the spoke width is widened to 35 µm. The undercut decreases the effective capacitance as the silicon is removed and replaced with air, thereby, allowing wider transmission lines in this region. Fig. 28(d) shows a closer view of the fabricated device.

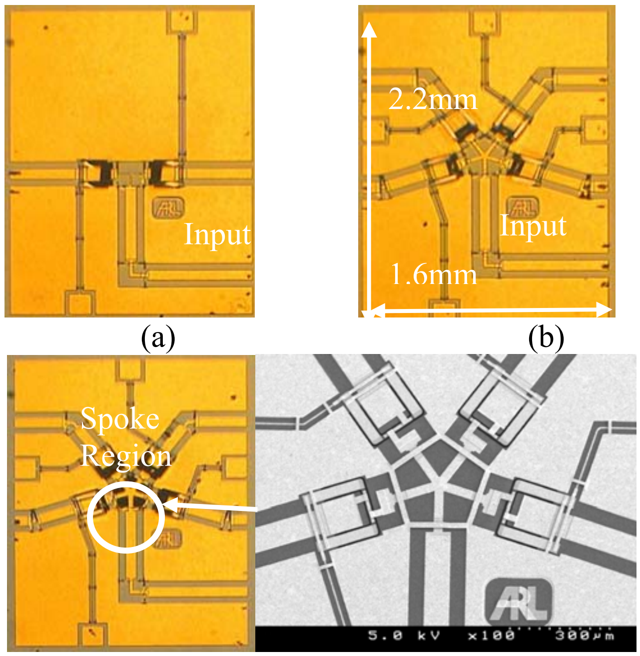

(a) (b)

(c) (d)

Fig. 28. Fabricated (a) SP2T (b) SP4T (c) SP4T with undercut indicated by the highlighted arrow and circle (d) Closer view of the SP4T.

Fig. 29 shows the measured response of the SP2T switches. The isolation is greater than 20 dB from DC to 50 GHz for both the S_{21} and S_{31} responses. Looking at Fig. 29(b), there is less than 2 dB of loss up to 40 GHz with an actuation voltage of 7 V. A DC current of 100mA is sent through the circuit in attempt to break through any residue that can be left on the contact point. The PZT switches have introduced parasitic capacitance and inductance as well as contact resistance that have not been accurately modeled in the initial simulations. Including accurate models of MEMS switches lead to memory problems and time consuming simulations that have been replaced with ideal modeling of the MEMS switches. We can conclude that there remains space for improving the matching of the SP2T switch, but the overall response reflects the advantage of using PZT switches in this application.

For the SP4T design, the isolation is greater than 20 dB up to 50 GHz similar to that of the single switch (see Fig. 30(a)). On average, the insertion loss is less than 1 dB at 20 GHz and about 2 dB at 40 GHz (see Fig. 30(b)). The return loss is greater than 15 dB up to about 30 GHz. Similar to the SP2T switch, the SP4T does not exhibit a great match at higher frequencies in contrast to the modeling predictions. Comparing to the simulated and estimate results, we have an additional 0.5 dB of loss to account for. Possible reasons include contact contamination from the fabrication process and discrepancies between the simplified simulation and the actual switch response. The additional loss is not a big deviation from the measured results and the overall response is well estimated with the simulations. The reflection still has room to improve with better modeling of the PZT MEMS switch in the SP4T simulation.

Fig. 31 shows the measured response with and without the undercut that is shown in Fig. 28(c). The darker colors represent the original measurement and the lighter colors show the response after the undercut. There is only a slight drop in the overall performance while being able to widen the spoke region to provide better RF power handling.

In conclusion, a SP2T and SP4T switch has been designed, fabricated, and measured taking advantage of the great RF characteristics of PZT MEMS switches. With high isolation and low loss beyond 40 GHz along with a low actuation voltage of 7 V, the SP2T and the SP4T switch show promising use for RF applications, such as phase shifters and phased arrays. The isolation is below -20 dB from DC to 50 GHz and the insertion loss is less than 1.8 dB up to 40 GHz for the SP2T and less than 2 dB up to 40 GHz for the SP4T.

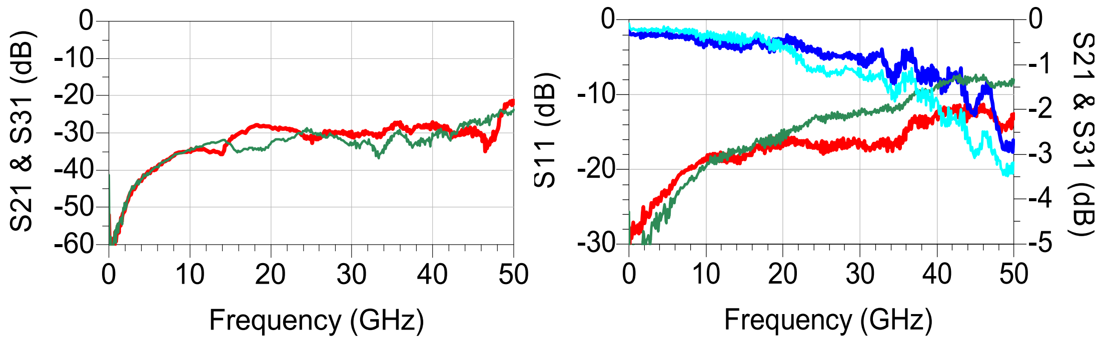

Fig. 29. Measured SP2T response of (Top) isolation, (Bottom) insertion loss, and return loss.

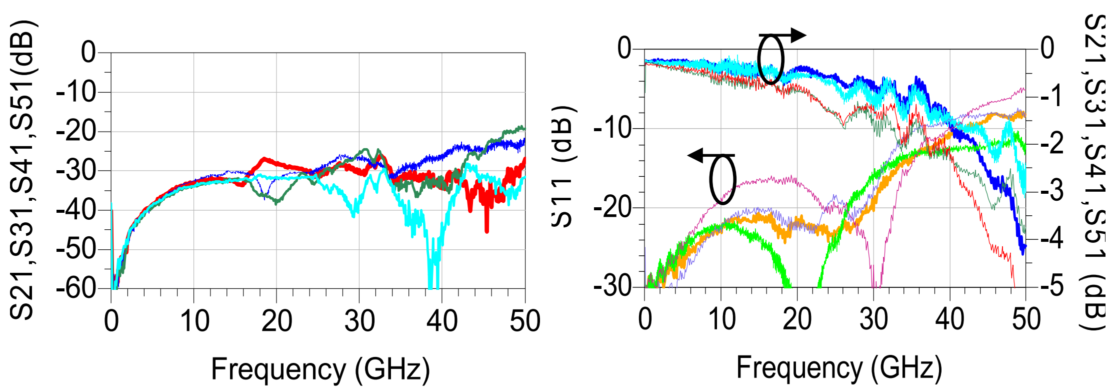

Fig. 30. Measured SP4T response of all ports. (Top) isolation, (Bottom) insertion loss, and return loss.

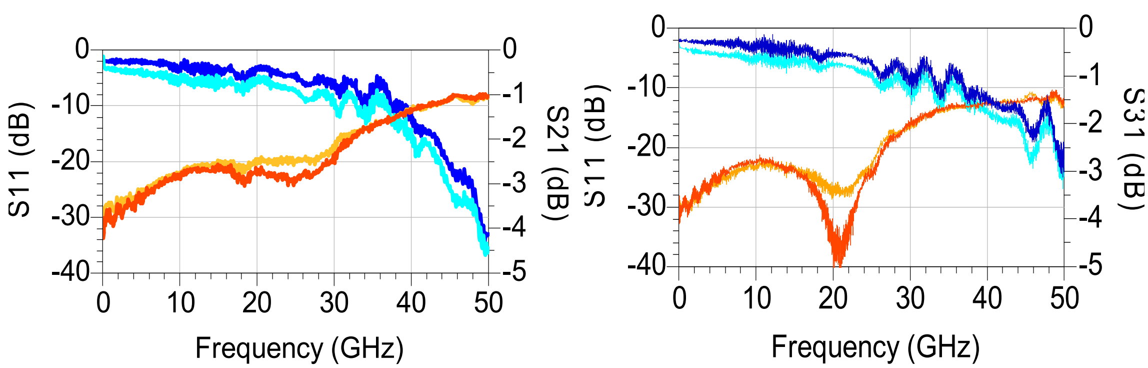

Fig. 31. Measured SP4T response with (light) and without (dark) under cut. (Top) port 2 actuated (Bottom) port 3 actuated.

During this project we also developed low loss X-band phase shifters on organic LCP substrates utilizing the low voltage PZT MEMS switches for the first time. Previous work has shown the routing of the delay lines on multiple layers of LTCC for isolation purpose, but at a higher cost and limited integration compatibility for large antenna arrays. Hybrid integration of a RF MEMS phase shifter on polymers has been shown, however, with high voltage SP2T switches and high insertion loss. This work uses silicon based lead zirconate titanate (PZT) MEMS switches in a SP4T configuration embedded in a multilayer LCP stack up for a low voltage compact delay line phase shifter at 10 GHz.

In order to achieve maximum compactness, SP4T switches are used in the design of the phase shifters because they are more compact and reduce the number of switches in the signal path compared to using SP2T switches. Fig. 32 shows the top view layout of the proposed hybrid multilayer design in comparison to a single layer design. Overall, a 22.5% reduction in footprint is achieved with the multilayer design as the embedded ground is able to isolate any of the overlapping lines. The delay lines of the phase shifter are given in 90° phase increments where each line length is estimated by (1).

$$l_n = l_o + n \cdot \frac{\lambda}{4} \qquad (1)$$

where l_n is the length of the nth line in reference to l_o (the 0° line) and n refers to the 90·n° line. λ is the wavelength on LCP, which is approximately 17.3 mm at 10 GHz. The 90° phase difference among elements gives the maximum beam steer for antenna arrays with λ/2 spacing, which is most common.

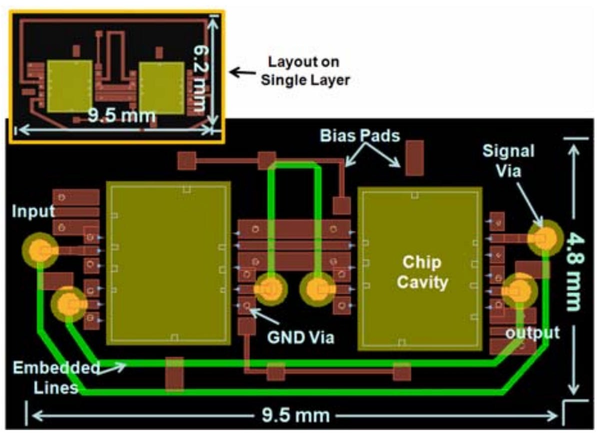

Fig. 32. Layout of the 3D phase shifter with a size comparison to a phase shifter with its foot print on a single layer.

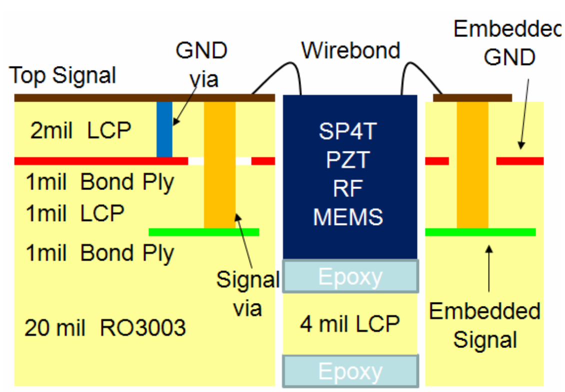

Fig. 33. Stack up of the 3D phase shifter design.

Once the estimated line length is calculated, ADS Momentum is used to further optimize the design to include the effects of bends, wirebonds, and via transitions. The lines on LCP are Grounded Co-Planar Waveguide (CPWG) lines to match the CPW lines on the SP4T chip. The embedded lines however, are microstrip lines, requiring simple CPWG to microstip transitions. The embedded microstrip lines are mitered at the bends and the width needs to be optimized to compensate for the additional parasitic capacitance and inductance from the via transitions. Fig. 33 shows the stack up of the multilayer design. The bond ply material has the same electric properties but a lower melting temperature (285^{o}C) compared to the core LCP (315^{o}C), which allows the bonding of multilayer stack up. The 20 mil RO3003 is an organic material with similar electrical properties that is chosen for the purpose of creating a cavity and embedded layers. The ground vias are 4mil diameter and the signal vias are 8 mil diameter with a diameter to height ratio of 2:1. The landing pad for the signal via is 16 mil diameter and the anti-pad in the embedded ground is 24 mil diameter to give 4 mil around each circle for fabrication tolerances.

The silicon PZT SP4T chips are 21 mil thick and they are mounted in a cavity with silver epoxy and wirebonded out to the top signal lines. In addition, the chips are placed on a small piece of 4 mil LCP to level the SP4T chip surface to the top signal layer on LCP for minimal wirebond length.

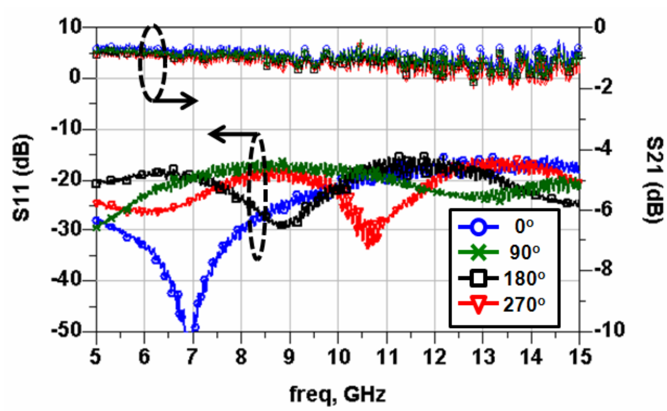

Fig. 34. Simulated return loss and insertion using measured SP4T response.

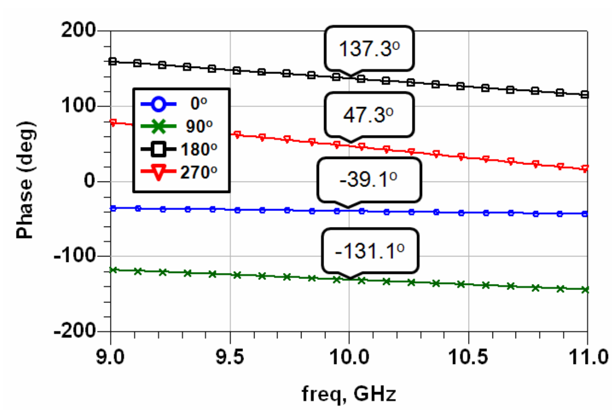

Fig. 35. Simulated phase response.

Fig. 34 shows the simulated response of the phase shifter with the measured SP4T chips but excluding the wirebonds. The return loss is greater than 18 dB and the average insertion loss is 1.22 dB. Fig. 35 shows the simulated phase response.

The PZT MEMS switches are fabricated at the US Army Research Laboratory (ARL) using their process. The LCP multilayer design is processed on a 18 inch by 24 inch panel with 75 µm minimum features. The fabricated and assembled 3D phase shifter is shown in Fig. 36. One mil wirebonds are used to connect the SP4T chip to the lines on LCP. Though the PZT MEMS actuate at 7 V, a 10 V bias is used for actuation to achieve a higher contact force, which improves the insertion loss. Higher contact force results in a lower contact resistance for the ohmic contacts.

Fig. 37 shows the measured return loss and insertion loss of the 3D phase shifter. At 10 GHz, the worst case is the longest phase line with 1.66 dB of loss and the best case is the shortest phase line with 1.17 dB of loss. On average, the line loss is 1.5 dB, which amounts to 0.75 dB/bit. The return loss shows that the device is well matched at 10 GHz with better than -18.3 dB. The performance of the phase shifter above 11 GHz declines despite the fact that the SP4T switch and via transitions have wide band performance beyond 20 GHz.

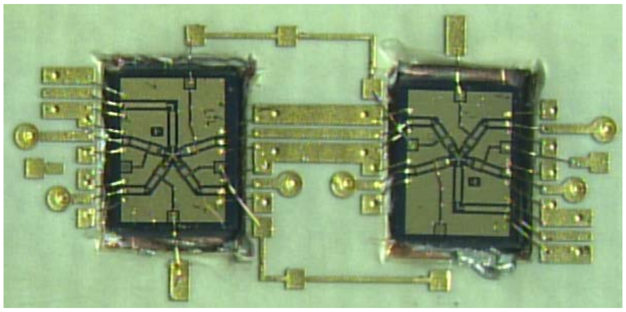

Fig. 36. Fabricated and assembled device.

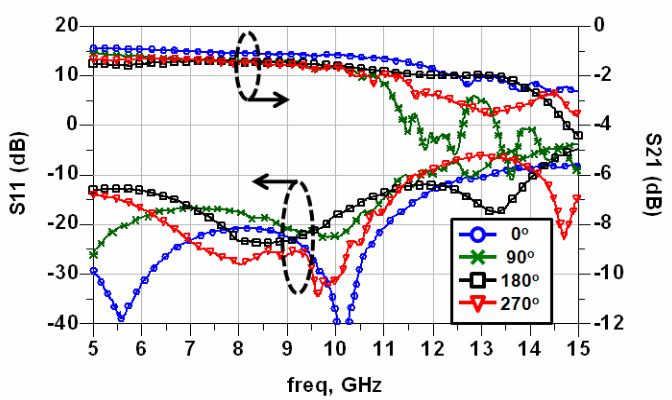

Fig. 37. Measured return loss and insertion loss of 3D phase shifter.

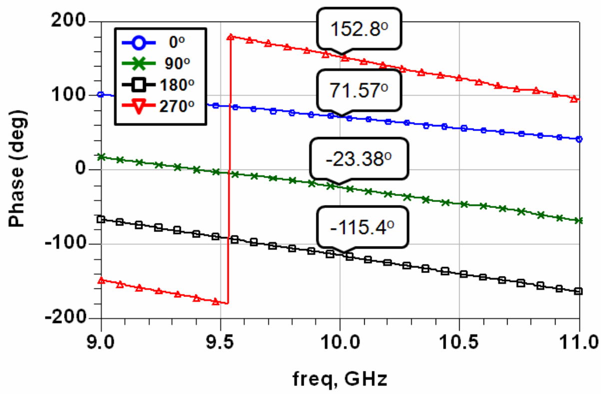

Fig. 38. Measured phase response of 3D phase shifter.

This is due to the long wirebonds that are measured to be longer than 600 μm. As the frequency increases, the effective parasitic resistance and inductance of the thin wirebonds increase as well, resulting in higher loss and worse matching. Reducing the length or using thicker wirebonds, preferably ribbon bonds can help improve the performance at higher frequencies. The measured phase response for each 90^o incremental state is shown in Fig. 38. The average phase error for each state in reference to the 0^o state is 2.15^o. The performance of the phase shifter is summarized in Table V.

The loss and size can be further improved by reducing the overcompensated size of the cavity, which leads to shorter wirebonds with less parasitic effects. In addition, if the SP4T switches are made application specific, the size of the MEMS chip can be reduced in half so that the cavity size is further reduce and the line loss on chip decreases. The result of these corrections leads to at least another 15% additional reduction in size and more than 0.3 dB improvement in insertion loss.

TABLE V
SUMMARY OF PHASE SHIFTER PERFORMANCE AT 10 GHZ

	Worst Case	Average	Best Case
Simulated S21 (dB)	-1.39	-1.22	-1.04
Simulated S11 (dB)	-18.95	-21.86	-23.6
Measured S21 (dB)	-1.66	-1.5	-1.17
Measured S11 (dB)	-18.3	-20.4	-31
Phase Error (^{o})	4.85	2.15	1.69

In conclusion, a compact, lightweight, multilayer 2-bit phase shifter using hybrid integration of a low voltage PZT RF MEMS and low cost LCP is shown for X-band phased antenna array applications. The phase shifter achieved 0.75 dB/bit insertion loss with 2.76^o rms phase error at 10 GHz using 10 V for actuation. In addition, compared to a single layer layout, the proposed 3D phase shifter is 22.5% smaller. The low voltage and multilayer process gives the phase shifter great potential for system level integration for RF front end applications.

5.0 UWB Elliptical Monopoles with a Reconfigurable Band Notch Using MEMS Switches Actuated Without Bias Lines

5.1 Introduction

The rapidly increasing number of wireless applications has led to a very heavy congestion in the available RF and wireless spectrum, causing significant interference among the different users and degrading the performance of the affected radios. To overcome this problem in an opportunistic way, agile radios are required that demand the use of “smart”, reconfigurable antennas capable of canceling in-band interference. Since the ultra wideband (UWB) radios share part of the spectrum with the HIPERLAN/2 applications (5.15-5.35 GHz, 5.470-5.725 GHz) and the wireless local area network (WLAN) applications using the IEEE 802.1la (5.15-5.35 GHz, 5.725-5.825 GHz) protocol, an ultra wideband antenna with reconfigurable band-rejection characteristic at the WLAN frequencies is highly desirable.

Several designs of UWB antennas with band rejection characteristics have been investigated and successfully implemented in the past. In this work, two CPW-fed elliptical monopoles were fabricated on LCP with reconfigurable rejection band (band-notch) characteristics in the frequency range between 5 and 6 GHz (HIPERLAN/2 and WLAN frequency range). The first antenna uses a $\lambda/2$ long, U-shaped slot and the second antenna uses two symmetrically placed $\lambda/4$ long, inverted L-shaped stubs as resonating elements. Micro-electro-mechanical system (MEMS) switches were used to activate and deactivate the resonating elements without the need of DC bias lines due to a novel design of the switch geometry. Transmission line models and surface current distributions were also used to explain the effect of the added resonating elements. The antennas can be mounted and conformed on the Army's unmanned ground vehicles ("bots") for wireless communications.

5.2 Antenna Design

The UWB antenna used for the integration of the reconfigurable "band-notch rejecting" elements is a CPW-fed elliptical monopole fabricated on 100 μm thick LCP (ε_r= 3, tanδ=0.002). The LCP samples were polished to reduce the surface roughness and allow for the MEMS switch fabrication. The two fabricated prototypes are presented in Fig. 39.

The elliptical radiator has a major axis A=18 mm and a secondary axis B=15.30 mm. Figure 40 presents the details of the schematic design and its dimensions are summarized in Table VI. The overall width of the antenna, W_{g1}, is 26.88 mm and the ground length is L_g=20.7 mm. A CPW feed line with central conductor width W_{f2}=3.89 mm and ground-signal gap G_2=100 μm is used, resulting in a characteristic impedance (Z_o) of 50 Ohms. In order to use 850 μm pitch probes for measurements, the CPW line is linearly tapered down to a narrower CPW line with 50 Ohm characteristic impedance (W_{f1}=1.28 mm and G_1=50 μm) that had length only L_1=1 mm . A customized transition from the standard CPW line (W_{f2}, G_2) to the ellipse was used to improve the matching. The matching improvement can be seen in Fig. 41 where the input impedance of two antennas, one referred to as "Standard CPW" and one referred to as "Reference" are presented on a Smith chart. The "Standard CPW" does not use any CPW-radiator transition; a standard, uniform width CPW line with the above mentioned geometrical characteristics (W_{f2}, G_2) is terminated with the elliptical radiator. The "Reference" is identical with the antenna presented in Fig. 40 without the slot or the two open stubs. It is referred to as "Reference" because it will be compared to the antennas with the reconfigurable resonating elements. Figure 41 shows that a uniform CPW line cannot establish good matching for this elliptical monopole, but the use of an appropriate CPW to radiator transition can achieve a SWR less than 2 across the whole UWB range. The two lines represent measurements taken between 2 to 12 GHz. The segment of the "Reference" line that falls outside the SWR=2 circle corresponds to the frequency range from 2 GHz to 3 GHz, which is not part of the UWB frequency range.

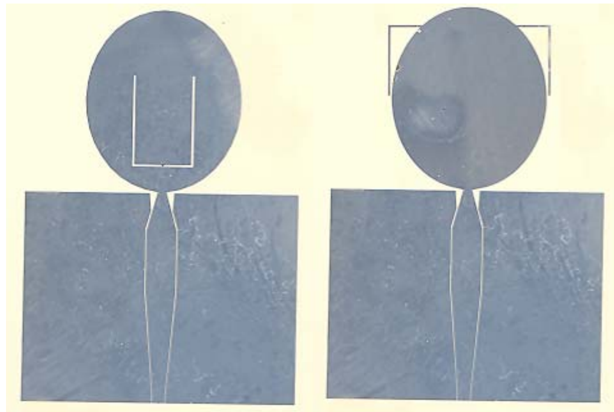

(a) (b)

Fig. 39 Fabricated antenna prototypes on LCP organic substrate with RF MEMS switches.

Table VI Antenna schematic dimensions

L_1	1.00 mm	W_{S2}	3.41 mm	W_{f3}	0.85 mm
L_2	10.00 mm	G_{S2}	0.20 mm	S_1	0.70 mm
L_3	6.00 mm	L_{S2}	6.80 mm	G_1	0.05 mm
L_4	1.93 mm	D_2	1.80 mm	G_2	0.10 mm
L_5	3.70 mm	W_{g1}	26.88 mm	G_3	0.11 mm
W_{S1}	5.60 mm	W_{g2}	12.25mm	L_g	20.70 mm
G_{S1}	0.20 mm	W_{f1}	1.28 mm	A	18.00 mm
L_{S1}	8.8 mm	W_{f2}	2.97 mm	B	15.30 mm
D_1	2.60 mm				

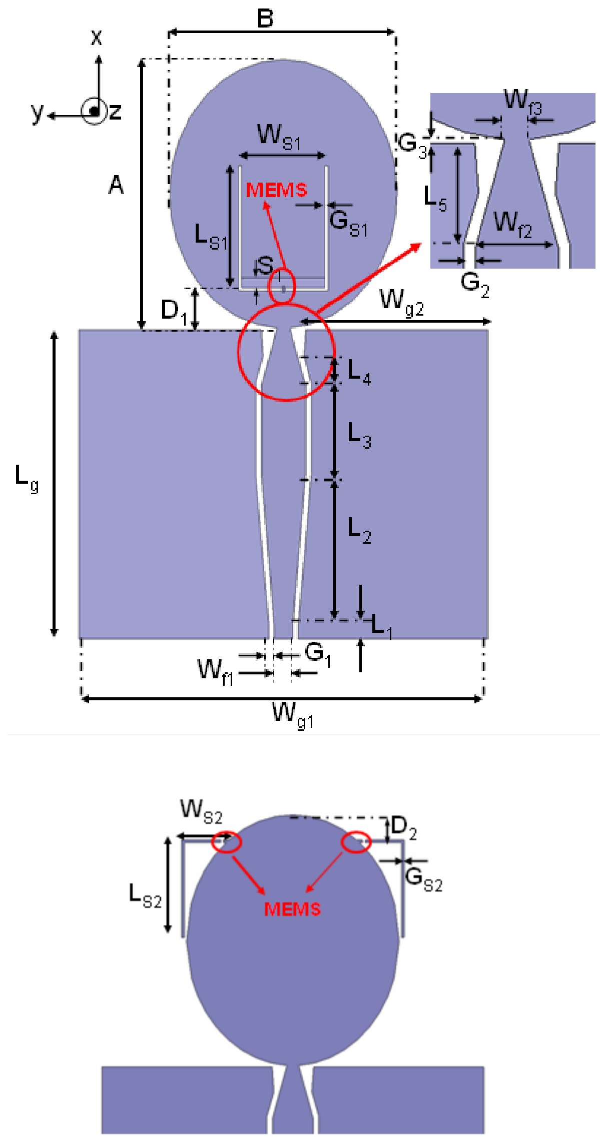

Fig. 40 Antenna schematic

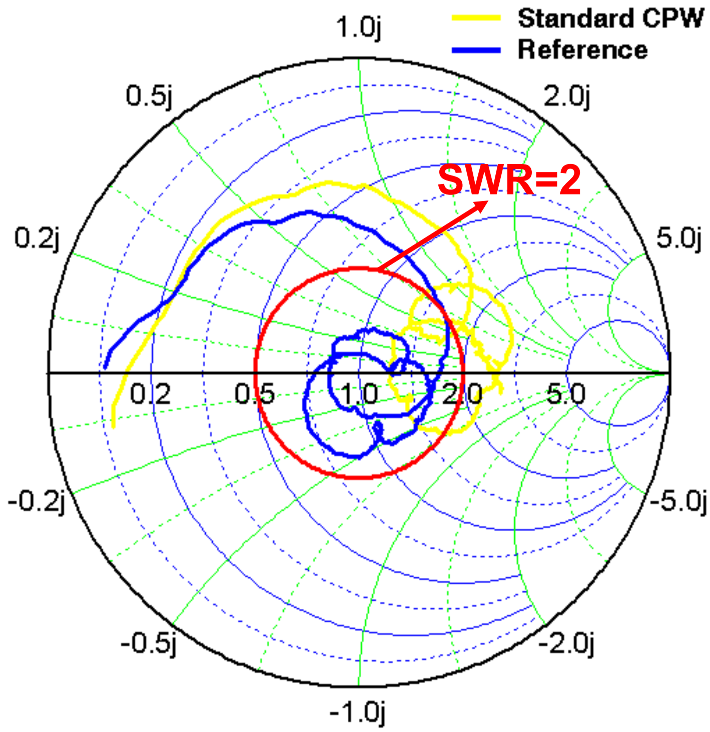

Fig. 41 Input impedance for "Standard CPW" and "Reference" antennas on Smith chart.

Two different approaches (a U-shaped slot and two inverted L-shaped open stubs) are demonstrated to achieve a reconfigurable band notch between 5.2 and 6 GHz. The U-shaped slot is presented in Figs. 39a and 40a. It consists of two parallel segments of length L_{S1}=8.8 mm and a third segment with length W_{S1}=5.6 mm that is positioned D_1=2.6 mm from the nearest ground edge. In the middle of this third edge and along the symmetry plane of the antenna, a MEMS switch is integrated to selectively short the 0.2 mm wide slot. Another very thin slot (only 3 µm wide) is created parallel to the third segment at a distance S1=0.7 mm from it. Therefore an isolated rectangular segment is defined which serves as the floating DC ground, which is necessary for the MEMS switch actuation. For the design shown in Figs. 39b and 40b, two inverted L open stubs with width G_{S2}=200 µm and total length 10.41 mm (L_{S2}+W_{S2}+G_{S2}) cause the band notch. Both stubs are placed at a distance D2=1.8 mm from the top point of the ellipse. Two MEMS switches are used to electrically connect and disconnect the two stubs to the elliptical radiator. The switches are positioned 0.4 mm from the ellipse. Bias lines are not needed in neither the slot nor the stubs case for the MEMS switch actuation because of the switch topology.

5.3 Operation Principles

For both antennas, the reconfigurability relies on the same concept of adding or removing a resonating structure. For the U-shaped slot antenna, the total length of the slot is approximately λ/2 at the frequency at which the rejection band is desired if the MEMS switch is up or open, and the MEMS switch shorts the slot at the center, which eliminates the resonance around 5 GHz. For the open stubs antenna, the two L-shaped, open circuit terminated stubs have a length approximately λ/4 at 5.8 GHz resulting in resonating elements that prevent radiation if the MEMS switches are down or closed, which connects the stub to the monopole.

A. Theory

The U-shaped slot resonates and therefore creates a band notch at the frequency that is related to its geometry dimensions as defined by: $f_U \sim \dfrac{c}{4\left(L_{S1}+\dfrac{W_{S1}}{2}-G_{S1}\right)}$ where c is the speed of light. The surface current distribution presented in Fig. 42a shows how the U-shaped slot resonates at 5.8 GHz and how this behavior is cancelled when the slot is shorted (Fig. 42b), or at a different frequency (8 GHz current distribution is presented in Fig. 42c). The directions of the current in the inner and outer side of the slot are opposite and they cancel each other. As a result, the antenna does not radiate at that frequency and a frequency notch is created around the frequency of 5.8 GHz. When the slot is shorted at its center point by the MEMS switch, the total length of the slot is divided in two and, consequently, it cannot support the resonating currents; thus, radiation occurs as if the slot was not present. A simple transmission line model is presented in Fig. 43 that explains the slot effect. The presence of the slot is modeled as a λ/4 long, short circuit terminated series stub, which is similar to a spurline filter. The MEMS switch is across the input to the series stub. If the switch is up, (Fig. 43a) the spurline filter is in the circuit, and at the stub resonant frequency, there is an equivalent series open circuit that reflects the signal. However, if the switch is down, the spurline filter is shorted, (Fig. 43b), or not in the circuit. Thus, radiation occurs at all frequencies.

Similarly the inverted L-shaped, open circuit terminated stubs resonate approximately at a frequency defined by: $f_{inverted\_L} \sim \dfrac{c}{4\left(W_{S2}+L_{S2}\right)}$ where again c is the speed of light. Fig. 42d shows how the two stubs resonate at 5.8 GHz. When the two stubs are not connected to the elliptical radiator no currents flow through the stubs (Fig. 42e) but even when they are connected they do not resonate at a different frequency (8 GHz current distribution is presented in Fig. 42f). At the resonance frequency, the direction of the currents on the inverted L stub and the current along the nearby edge of the radiator are opposite to each other. Therefore they cancel and the antenna does not radiate. Again a transmission line model is used to interpret the inverted L stubs effect on the radiation mechanism, where the presence of the two stubs is modeled as a λ/4 long stub. When the MEMS are in the "up" position, the stub is disconnected from the primary transmission line (Fig. 43c) and it has no effect on the incident power, which is radiated from the load ("antenna"). When the MEMS are in the "down" position the open stub appears as ideal short on the transmission line and the incident power is reflected as appears in Fig. 43d.

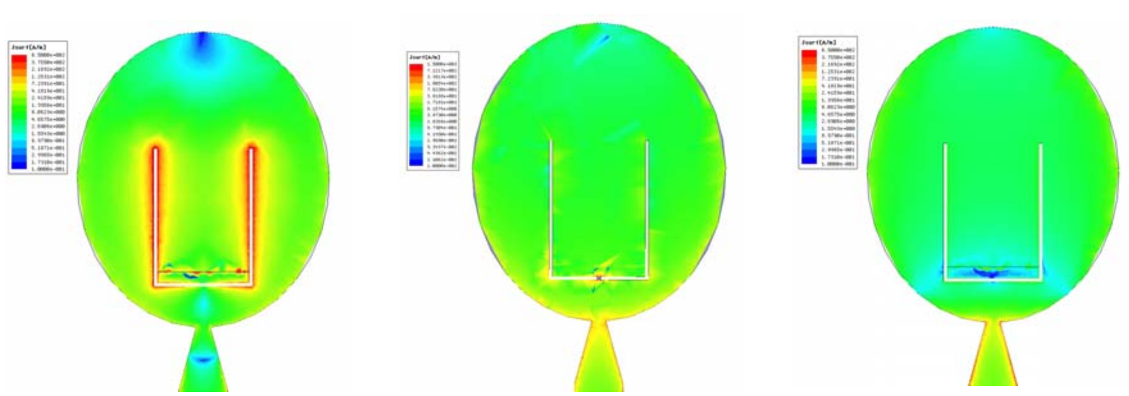

(a) (b) (c)

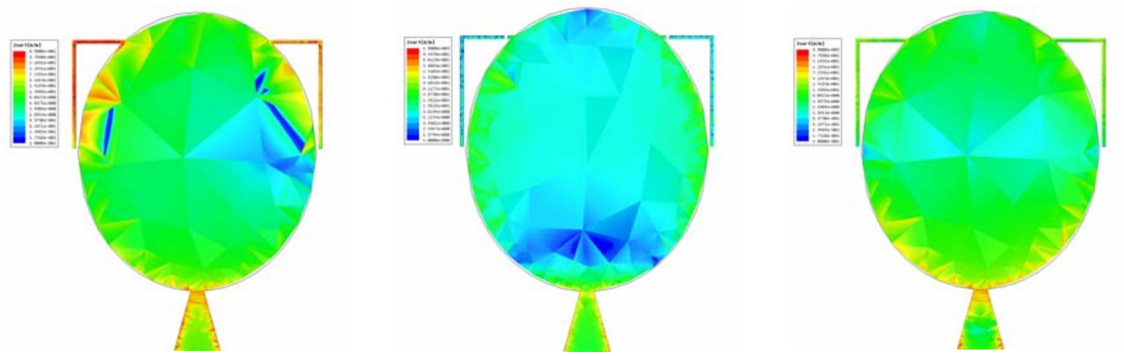

(d) (e) (f)

Fig. 42 Field distribution (a) Open slot at 5.8 GHz (b) Shorted slot at 5.8 GHz (c) Open slot at 8 GHz (d) Shorted stubs at 5.8 GHz (e) Open stubs at 5.8 GHz (f) Shorted stubs at 8 GHz.

B. Parametric Study

There is an inverse proportional relationship between the frequency of the band notch and the total length of the resonating elements as can be deduced from the approximate formulas presented in the previous section. This trend is verified numerically from the simulations presented in Fig. 44. Figure 44a shows the simulation results when L_{S1} varies for an antenna with a U-shaped slot when the additional thin slot (3 μm wide) is not present. This example is referred to as "Simple Slot". When it is compared with the antenna that uses the additional thin slot (similar to the schematic in Fig. 40) to create the isolated floating ground, which is referred to as "Thin Slot", it can be seen that longer length L_{S1} is required to have the frequency notch between 5 and 6 GHz (Fig. 44b) when the thin slot is present. Specifically for the "Simple Slot," L_{S1}=8.5 mm is required for a stopband at 5.8 GHz, whereas for the "Thin Slot," a little longer length of L_{S1}=8.8 is needed to cause a band notch in the same frequency range. Additionally, when the same length L_{S1}=8.5 is used for "Thin Slot" , the band notch shifts higher to approximately 6.0 GHz as can be seen in Fig. 44b. Similar behavior is observed for the length of the inverted L stubs, which is presented in Fig. 44c. The longer the length L_{S2} is, the lower the frequency of the band notch shifts. In each of the above simulations, all of the other dimensions are kept constant.

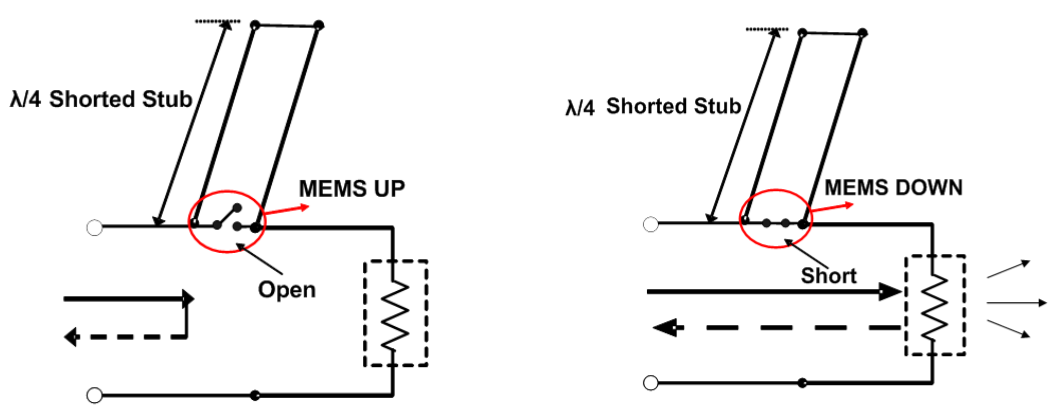

(a) (b)

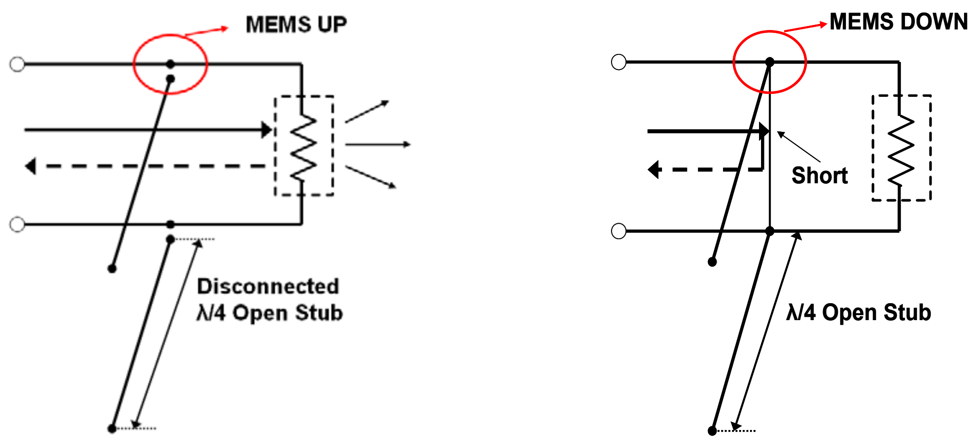

(c) (d)

Fig. 43 Transmission line model for (a) U-shaped slot with MEMS Up (b) U shaped slot with MEMS down (c) Inverted L stubs with MEMS up (d) Inverted L stubs with MEMS down.

Simulations show that another important parameter is the position of the resonating element, especially for the U-shaped slot. Figure 45 shows the simulated reflection coefficient for the two antennas as a function of the resonating element location. Figure 45a shows that the stopband frequency varies by 1.5 GHz if D_1 is varied by 1 mm. Furthermore, the magnitude of the reflection coefficient is seen to be dependent on the slot position, with a smaller reflection if D_1 is large. The large dependence on slot position is due to the strong currents at the elliptical radiator feed point, which couple strongly to the U-shaped slot. On the contrary, a small variation on the distance D_2 of the two L-shaped stubs from the top point of the ellipse does not seem to affect the band notch significantly. Figure459b shows that a 1 mm variation in stub location only causes a 750 MHz variation in stopband frequency. It is also noted that the magnitude of the reflection coefficient does not appear to be dependent on the stub location.

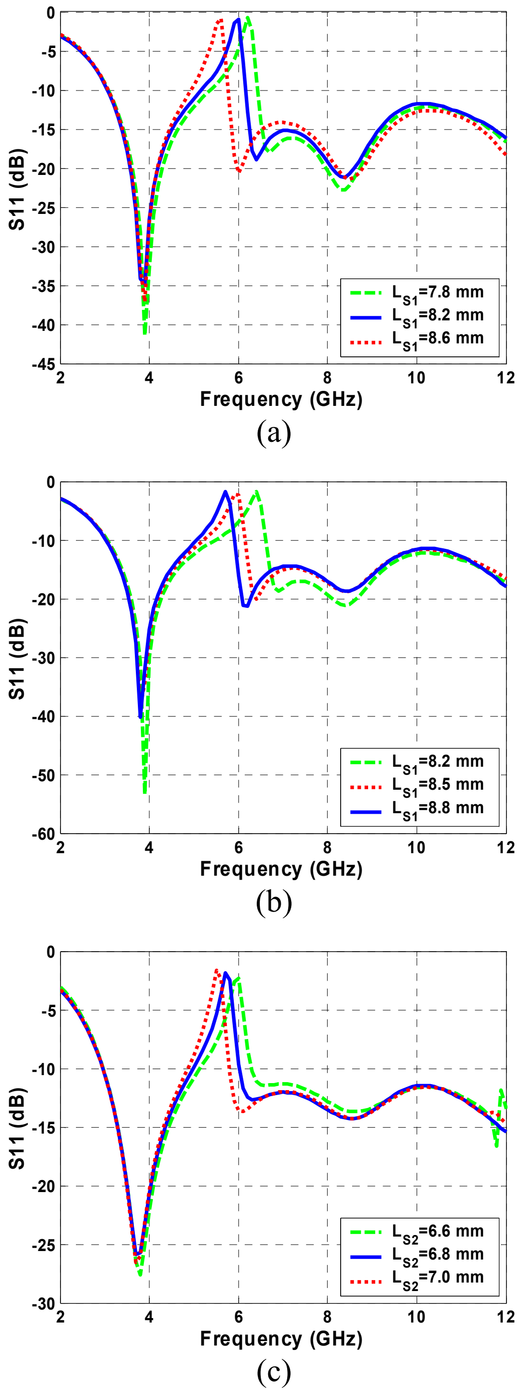

Fig. 44 Slot/Stub length effect on return loss (a) Simple slot, (b) Thin slot, (c) Stubs.

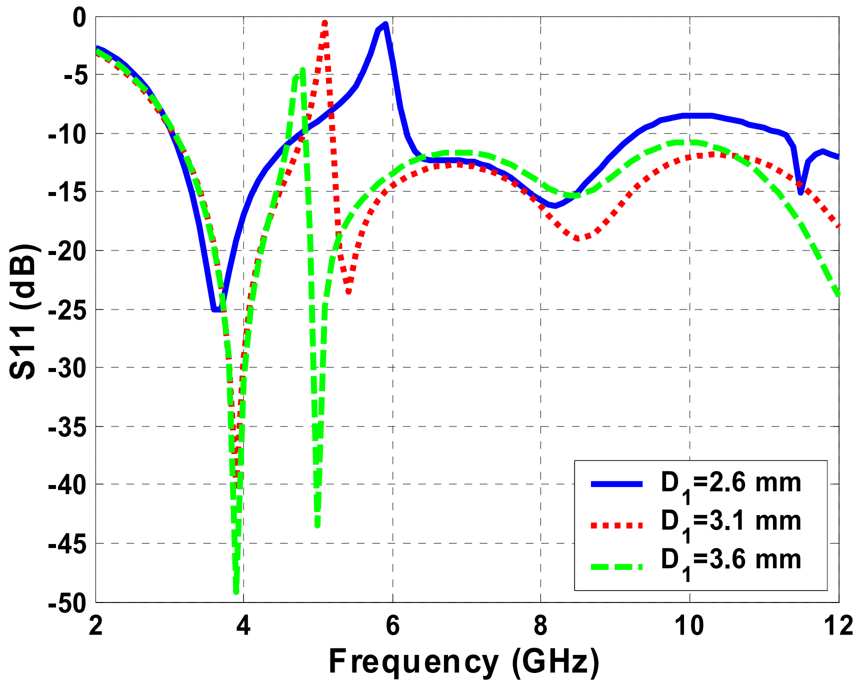

(a)

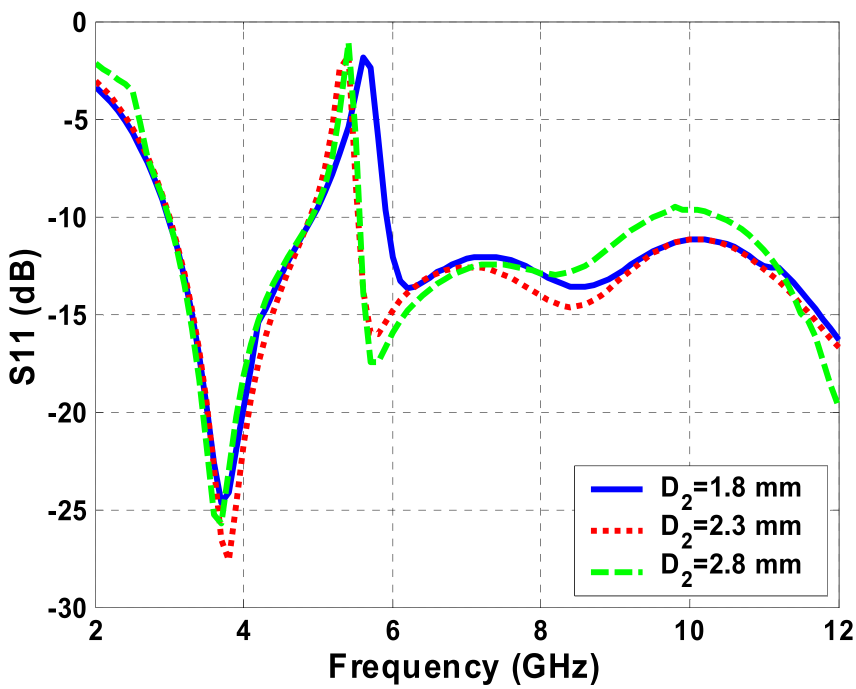

(b)

Fig.45 (a) Slot position effect, (b) Stub position effect.

5.4 MEMS Switches Operation and Integration

A. MEMS Switch Operation

MEMS switches were chosen for this application because of their low loss, excellent isolation, and wide-band response. The challenge with MEMS switch integration in an antenna system is with biasing the switches without affecting the radiation characteristics. To avoid this issue, a new biasing technique was implemented. For this technique to work, there must be a DC short between the signal line input (center pin on the CPW antenna feed) and the posts of the MEMS switches. This method also requires that the MEMS are Ohmic and single-supported.

The DC actuation voltage is applied directly to the CPW center pin through a DC bias on the vector network analyzer. When no voltage is applied, the switches are in the up position and the antenna exhibits one behavior. When a voltage is applied, an electrostatic force pulls down the MEMS switches and since they are Ohmic, they create a DC and RF short at the contact point. The antenna now exhibits a different behavior.

Since there is a DC short between the signal line input and the posts of the MEMS switches, no additional metal lines are required to apply the actuation voltage. To avoid the addition of DC ground lines, a floating ground is used. In this method, a metal pad beneath the switch is not shorted to anything. It does not represent a true ground, but it is sufficient to provide a foundation for electrostatic force generation. The pad is isolated from direct contact with the switch membrane by a thin layer of silicon nitride. To avoid failures due to dielectric charging, this method should only be used in systems that will be continuously reconfigured. The MEMS switch geometry is shown in Fig. 46.

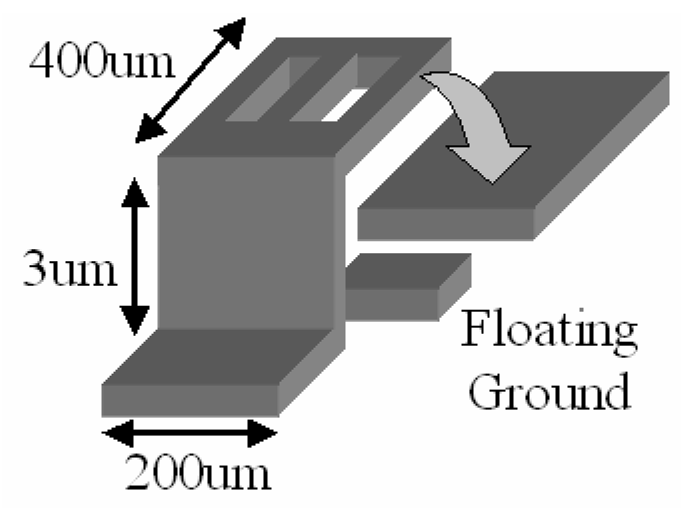

Fig. 46 The MEMS switch geometry and floating ground concept are shown.

B. MEMS Switch Integration

Fabrication and MEMS integration was performed in six general steps. First, the LCP material was polished using alumina slurry until the surface roughness was approximately 10nm. This roughness is comparable to that of a polished silicon wafer. Therefore, the original polymer roughness has no effect on the switch or the antenna performance. Second, the bottom seed layer was electron-beam deposited. Third, a silicon nitride layer was deposited using Plasma Enhanced Chemical Vapor Deposition (PECVD), patterned, and etched using a Reactive Ion Etch (RIE). Fourth, a sacrificial photoresist layer was patterned to define the switch height (3 μm). Fifth, a 1.5 μm thick Ti-Al layer was electron-beam deposited and etched to define the switch membranes. Lastly, the switches were released by soaking in photoresist stripper and dried using CO_2 at the supercritical point. A picture of a fabricated MEMS switch is shown in Fig. 47. This switch geometry with a floating ground has an actuation voltage of less than 30V.

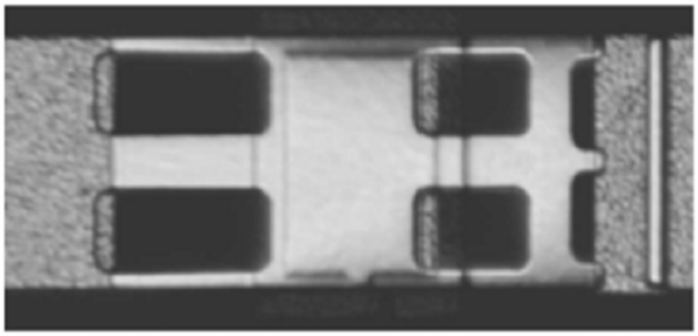

Fig. 47 The fabricated MEMS switch is shown. The post is located on the left and the ohmic contact is made on the right.

5.5 Measurements and Discussion

A. Return Loss Measurements

For the return loss measurements, an Agilent 8510 vector network analyzer was used and the input signal was launched through 850 μm pitch GSG probes. The DC voltage for the MEMS actuation was applied through the RF cable that connects to the network analyzer and it follows the same path with the RF signal. An S_{11} measurement was taken when the MEMS were "up" (OFF state) without applying any DC voltage and another measurement was taken when 28 V DC voltage was applied and the MEMS' bridge went down, switching to ON state. The return loss measurements are compared with the "Reference" antenna, which is a sample without any resonating elements. The measured S_{11} plots (Fig.48a) for the "Reference" antenna and the U-shaped slot antenna when the MEMS membrane is down (MEMS Down) are in very good agreement; when the switch membrane is in "up" position (MEMS Up) a frequency notch appears between 5 and 6 GHz. In Fig. 48b the same results are presented for the antenna with the inverted L stubs. The only difference is that the band notch appears when the switch is in "down" position (MEMS Down) and the "Reference" antenna has similar return loss behavior with the antenna with the switch not actuated (MEMS Up). The presented return loss measurements verify the good performance of the MEMS switches and the effectiveness of the suggested integration.

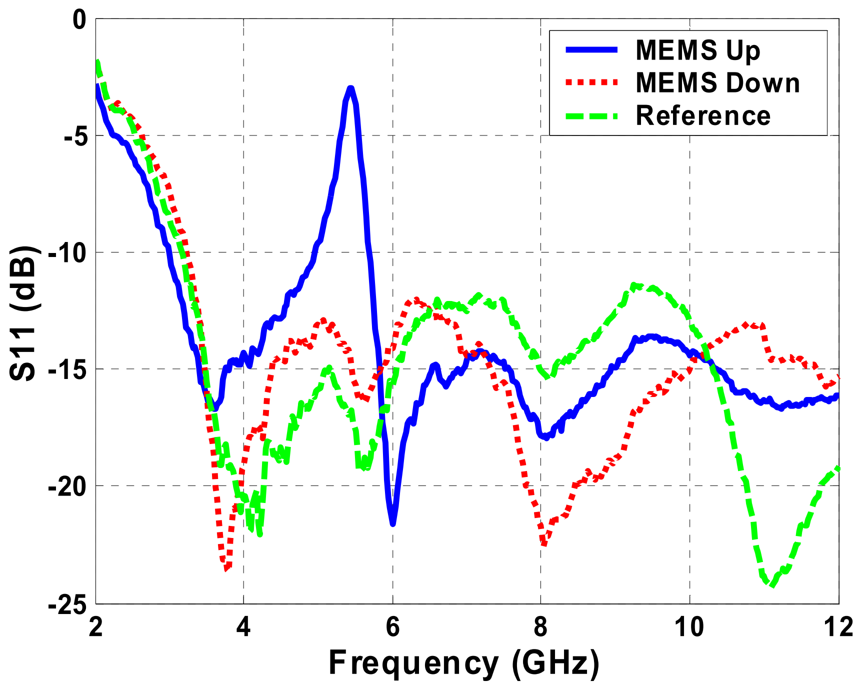

(a)

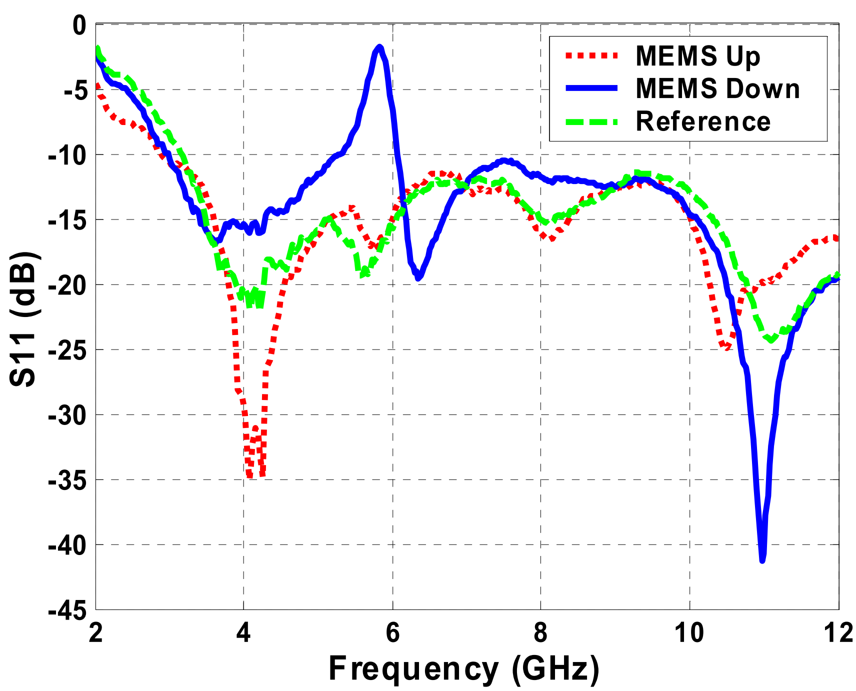

(b)

Fig. 48 (a) Return loss for antenna with MEMS reconfigurable slot, (b) Return loss for antenna with MEMS reconfigurable stubs.

B. Radiation Pattern Measurements

For radiation pattern measurements, instead of the antennas with the integrated MEMS switches, antennas were fabricated with hardwired interconnects where the OFF state was realized with an open circuit and the ON state was realized with a short circuit. The radiation patterns are measured on an antenna probe station measurement system that permits 360 degree of rotation with 850 mm pitch probes. However, even with a specially made GGP Industries probe with an extended microcoax section, the probe positioner and probe itself cause interference with the radiated fields. Therefore, only parts of the measured field patterns are shown. Measurements at 4 and 8 GHz are presented in both E (x-y) (Figs 49-50) and H (x-z) planes (Figs 51-52). The two states (shorted and open, which correspond to ON and OFF states of a MEMS switch) of the reconfigurable antennas are compared with the "Reference" antenna. In all cases the patterns are normalized independently. It is seen that the addition of the resonating elements does not significantly affect the radiation performance of the antennas.

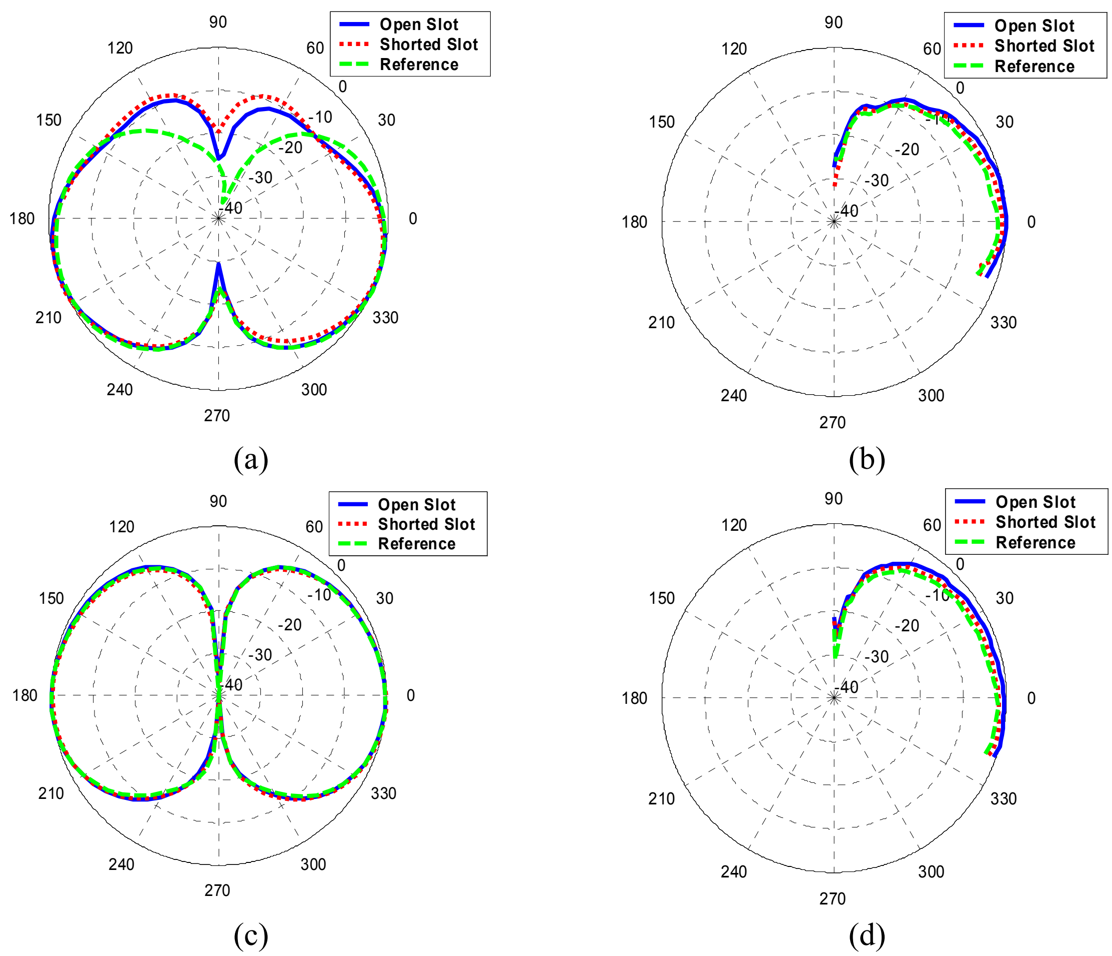

Fig. 49 U-shaped slot, E plane (a) Simulation at 4 GHz (b) Measurement at 4 GHz (c) Simulation at 8 GHz (d) Measurement at 8 GHz.

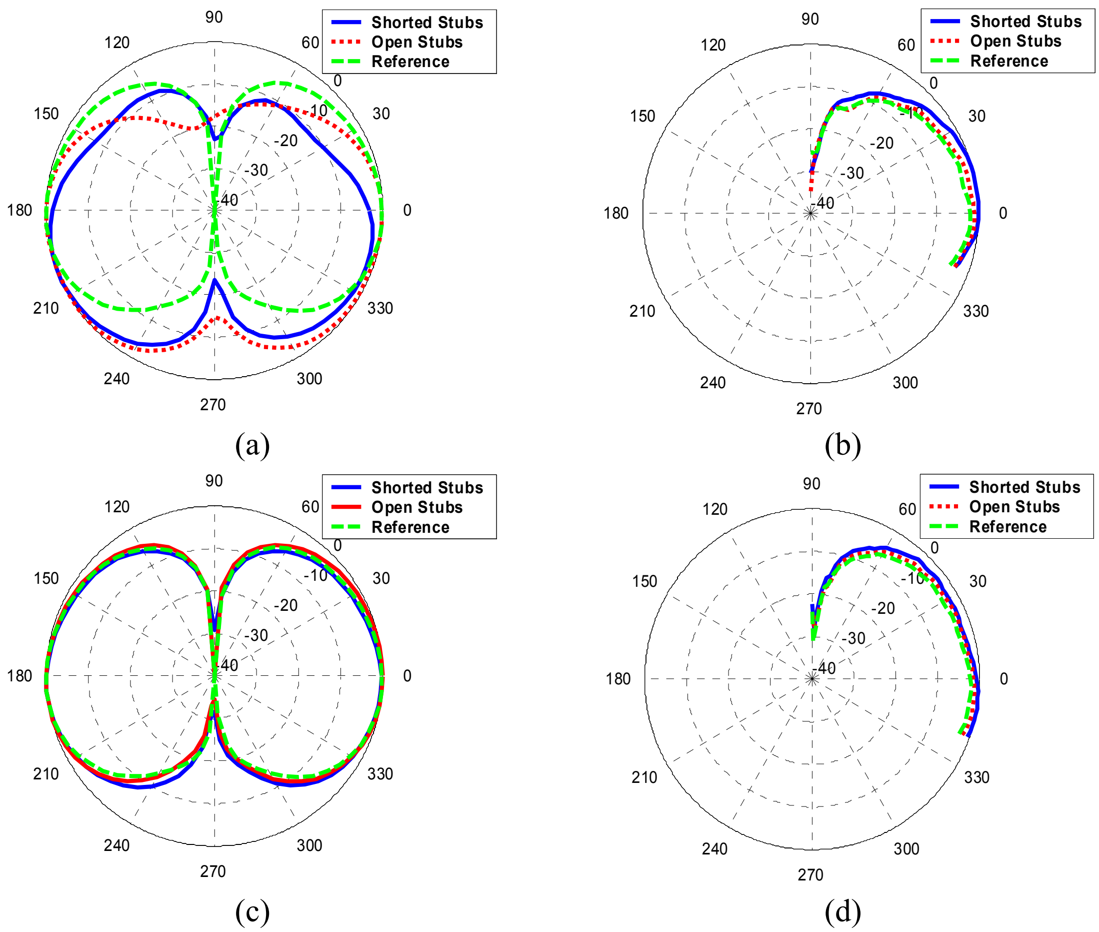

Fig. 50 L-shaped stubs, E plane (a) Simulation at 4 GHz (b) Measurement at 4 GHz (c) Simulation at 8 GHz (d) Measurement at 8 GHz.

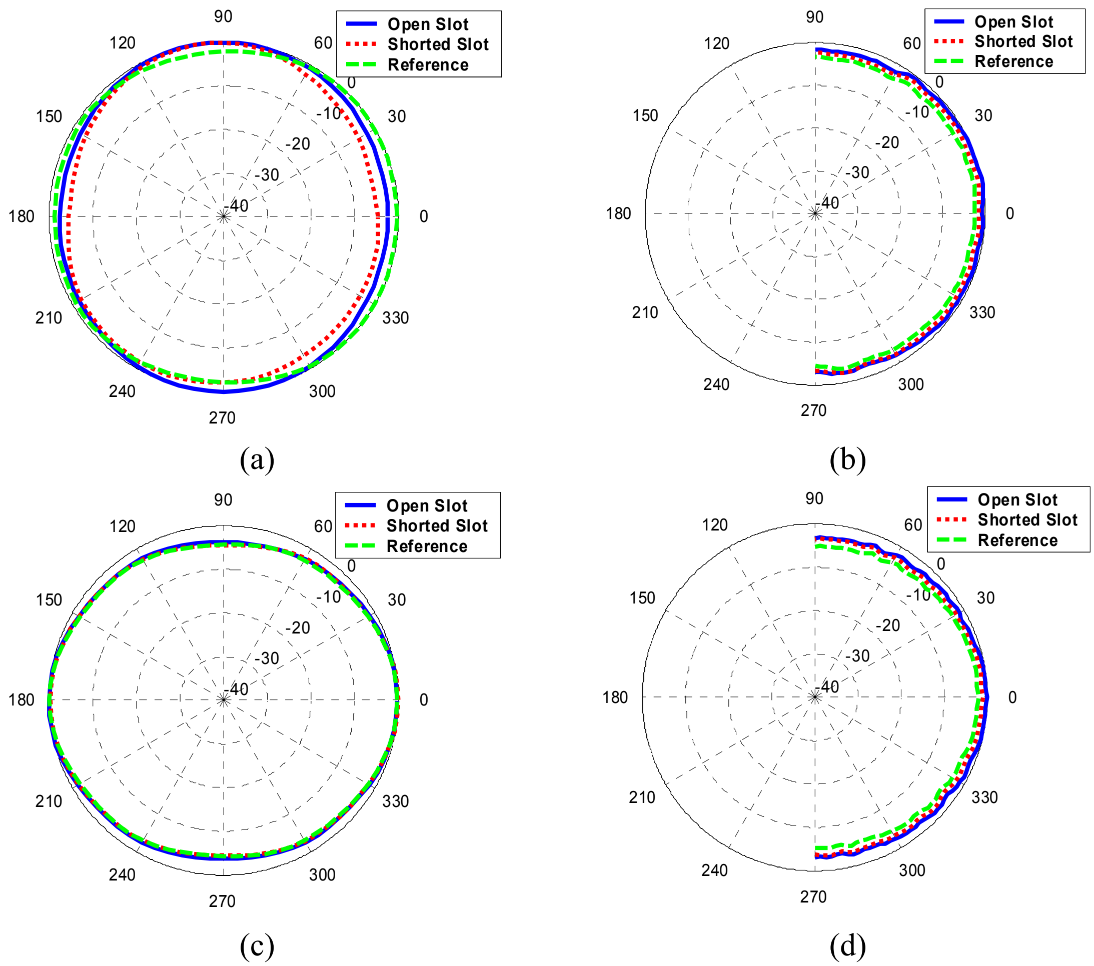

Fig. 51 U-shaped slot, H plane (a) Simulation at 4 GHz (b) Measurement at 4 GHz (c) Simulation at 8 GHz (d) Measurement at 8 GHz.

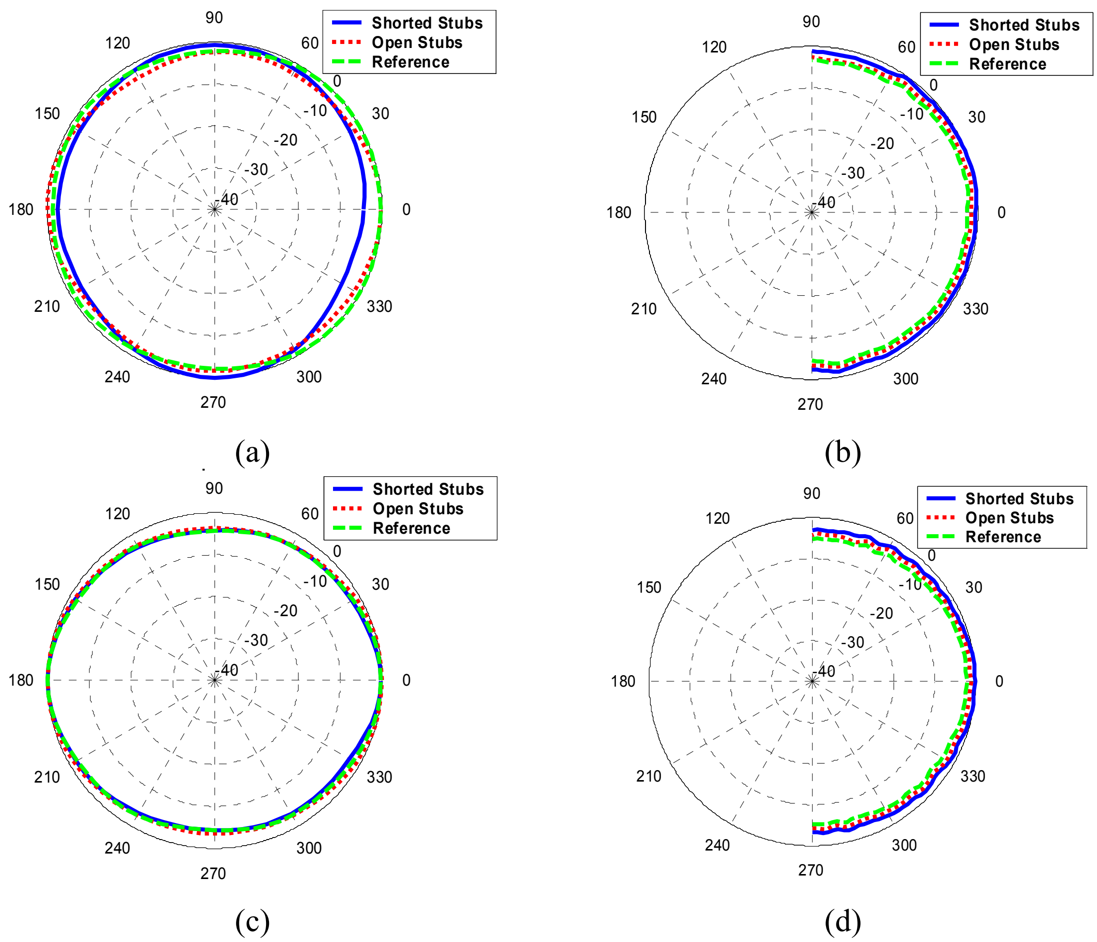

Fig. 52 L-shaped stubs, H plane (a) Simulation at 4 GHz (b) Measurement at 4 GHz (c) Simulation at 8 GHz (d) Measurement at 8 GHz.

C. Gain Measurements

The antenna gain was measured by using the substitution method. For the “known” antennas, open ended rectangular waveguides are used. The gain measurements shown in Fig. 53 were taken in the directivity direction which coincides with the z axis direction as it is defined in Fig. 40. As can be seen, the presence of the resonating elements and the frequency mismatch cause a significant degradation on the gain value at the frequency band to be rejected in a reconfiguring way. The antenna gain is suppressed by over 10 dB for the slot resonator and 6 dB for the stub resonator. The gain behavior over the remainder of the frequency band is similar for all three cases as can be verified from Fig 53.

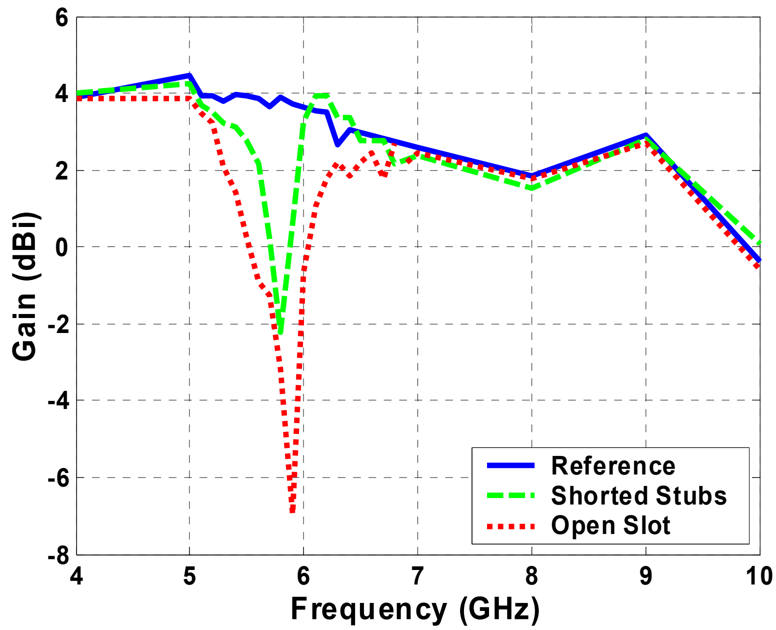

Fig. 53 Gain measurements.

6.0 Low Cost Organic Packaging for Silicon Based mm-wave Wireless Systems

LCP has excellent electrical and packaging characteristics up to 110 GHz that make it an ideal candidate for "wafer-scale" low cost organic packaging of mm-wave circuits. During the reporting period, we worked for the first time on embedding a mm-wave SiGe oscillator into an LCP organic material that acts both as substrate and package. Sufficient results showed that LCP can be successfully utilized to package an active device with minimal degradation in overall performance. In addition, it showed that LCP can be utilized as a multi-chip module platform.

The packaged circuit demonstrated is a voltage controlled oscillator operating at the upper end of Ka-band. Shown in Figure 54, the oscillator uses a cross-coupled negative resistance topology implemented in IBM's third generation SiGe technology node. The differentially configured common emitter stage creates a negative resistance across the collectors of the two HBT's by steering current back and forth between them. The circuit is made unstable by cross-coupling the base contacts to the opposing collector, ensuring that as random noise steers the current toward one transistor, the bias point of the opposite transistor increases steering the current back in the other direction. This oscillation will increase until the non-linearities of the transistor decrease the current gain to an equilibrium condition with the resonator.

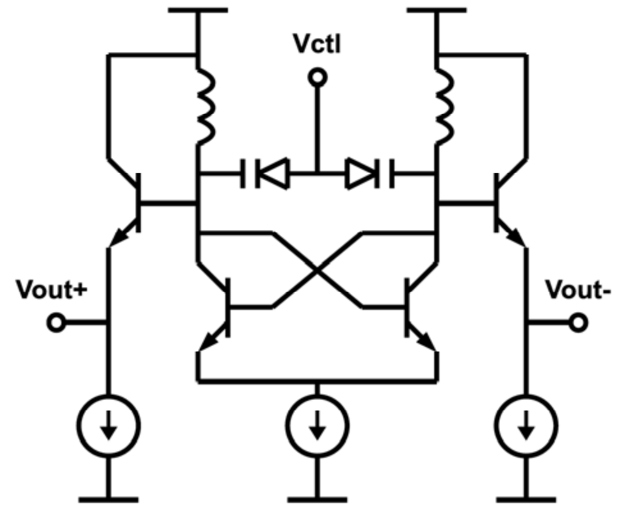

Fig. 54 Schematic of the negative resistance oscillator.

The negative resistance generated by the transistor pair is used to offset the loss of the resonator tank. The resonator sets the oscillation frequency of the VCO. In this circuit the resonator is formed monolithically, using a combination of varactors and metal lines. Adjusting the control voltage varies the effective capacitance of the varactor and adjusts the resonant frequency of the tank. The high impedance lines on the thick analog metal layer act as inductors with a much higher self resonant frequency than traditional spiral inductors. These state-of-the-art passive elements allow the circuit to push the frequency limits of this design topology. Emitter-follower buffers are used to extract the signal with minimal loading of the resonant tank. Since these buffers need to drive an inductive load in the form of package bond wires, care must be taken in the design to ensure that the amplifier is stable by adjusting the bias current and emitter scaling.

When measured at the wafer level without the package, the circuit achieves an output power of -13.6 dBm, with a phase noise of -94 dBc/Hz at a 1 MHz offset from the carrier frequency. The VCO has a tuning range of over 1 GHz, from 36.5 to 37.8 GHz. The measured oscillation frequency represents a 5% downward shift despite complete parasitic extraction during design. The VCO and buffer combined draw 13 mA on a 1.2 V supply. It is often convenient to combine several of these metrics into a common figure of merit that can be used to compare performance on an equal footing. A commonly used figure of merit to normalize phase noise is defined as:

$$FOM = \Phi_n(f_m) - 20\log\left(\frac{f_0}{f_m}\right) + 10\log\left(\frac{P_{diss}}{1mW}\right)$$

where $\Phi_n(f_m)$ is the measured phase noise at a given offset frequency, f_m. The oscillation frequency and DC power dissipation are represented by f_0 and P_{diss} respectively. Using this standard, the design shown here has a -173.7 dBc/Hz figure of merit.

The VCO was mounted in a laser ablated cavity on LCP. The corresponding chip pads were then wire bonded to the copper traces on the LCP. The general design of the packaging is seen in Figure 55.

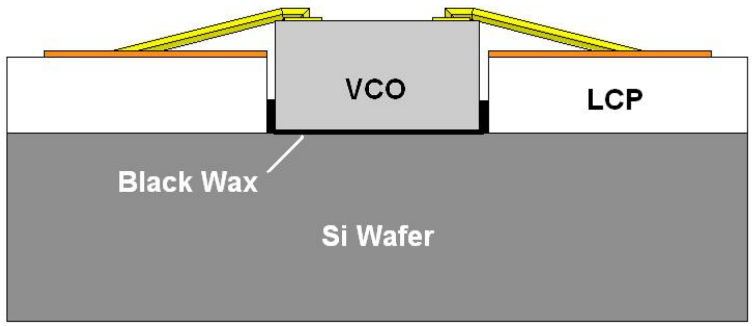

Fig. 55 Package design of chip mounted and wire bonded directly on to LCP.

The VCO chip was diced from its original wafer using a soft cutting blade with a 50um width. It was necessary to dice the chip as small as possible without damaging it in order to reduce wire bond lengths. After dicing, the chip dimensions measured 550um x 850um. For best packaging results, the dimensions of the cavity produced for mounting this chip will be approximately the same but slightly larger to allow for any errors. Before packaging, the VCO was measured on chip to ensure its integrity. The packaging material is a double copper laminated (metal thickness of 18um) 8 mil 3850 LCP sheet from Rogers Corporation. A mask was prepared for patterning the necessary transmission lines required for the VCO. The mask was designed with 120um line widths and 40um spacings. The transmission lines were arranged to allow for a cavity size of 600 um x 900 um. These dimensions are compensated for the degree of error produced when patterning copper traces on metallization layers 18 um thick. The transmission lines were patterned on to the LCP using photolithography and acetone was used to etch the copper. After etching, the line widths were about 90 um and the spacings were about 90 um. The final line patterns corresponded to the required 150 um pitch probes that would be used for measurement purposes. The copper backside of the package was unnecessary since the device did not require a floating ground connection. It was removed using photolithography and acetone etching.

Once the patterning was complete, a cavity for mounting the VCO needed to be cut. Since the VCO is slightly thicker than the LCP, the cavity needed to be cut completely through the LCP. This provided a near flush surface between the chip and LCP. Since LCP is a naturally flame retardant material, no halogen was needed to make the cut. The KrF 248nm UV excimer laser was used to ablate the cavity. This laser uses minimal heat to ablate the material at a high repetitive rate which gives a clean, precise cut on LCP without melting it and without affecting the copper traces. This allowed the cavity to be made as small as possible while minimizing the distance from chip to transmission line. The final cavity dimensions were 600um x 880um. Following the cut, the laser ablation left a residue of carbonized LCP around the cavity. This was removed using acetone and isopropyl alcohol. The final topology of the LCP is seen in Figure 56. Finally, a wire bonder was used to connect the SiGe VCO with the printed transmission lines on LCP. The bonder uses ultrasonic energy to make a weld between the contact points. This avoided the use of heat and excessive pressure which could possibly damage the component. Also by using the wedge wire bonder, the length of the wire bonds was minimal. The longest bond wire length was about 700 um and the average length was about 550 um. This helped to reduce the parasitic effects that are produced by this type of packaging. An image of the actual packaged circuit can be seen in Figure 57.

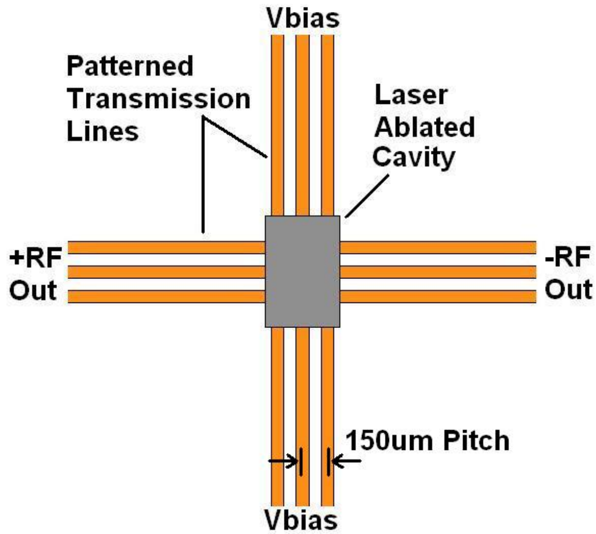

Fig. 56 Topology of patterned transmission lines and laser ablated cavity.

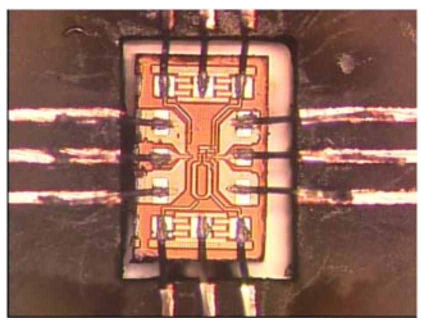

Fig. 57 Die photograph of the packaged oscillator.

Measurements of both the wafer level and package level oscillators were done on an Agilent E4446A spectrum analyzer. A Ka-band rat race coupler and phase tuners were used to combine the differential signal into single ended for measurement. A plot of the output spectrum of the packaged oscillator with respect to the unpackaged performance can be seen in Figure 58. Note that the x-axis has been normalized to the oscillation frequency. The increased parasitics of the packaged part causes an additional 1.9% shift in oscillation frequency. The output spectrums are overlayed to give a sense of the package loss and increased noise. The results show that the output power of the packaged part is 3 dB down from that of the unpackaged part, while the sidebands of the signal are noticeably higher in the packaged part. Tuning range of the VCO also suffers when packaged, decreasing by an order of magnitude from over 1 GHz to around 100 MHz. This also is caused by the increased parasitics that are largely inductive because of the bond wires. The increased inductance adds with the existing inductance and decreases the influence of the varactors on the tank circuit. The effect is large because the element values are small at Ka-band.

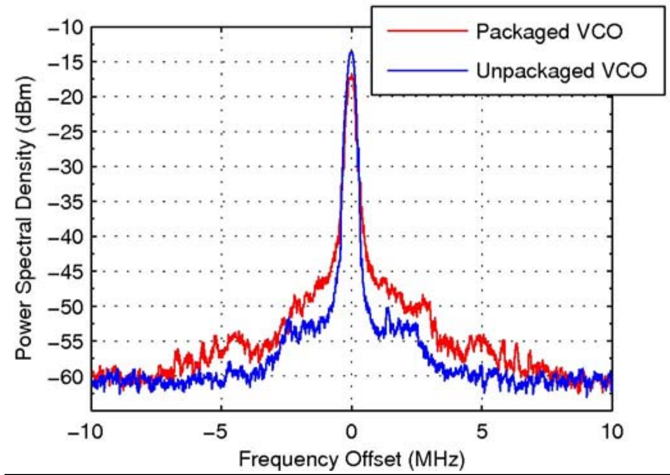

Fig. 58 Output spectrum of the packaged and unpackaged VCO. The x-axis is normalized to the oscillation frequency in order to overlay the plots, which shifted due to packaging parasitics.

Table VII PERFORMANCE SUMMARY OF THE PACKAGED AND UNPACKAGED VCO

Size	**Packaged VCO**	**Unpackaged VCO**
Output Power	-16.87 dBm	-13.64 dBm
Tuning Range	36.25-36.55 GHz	36.5-37.8 GHz
Phase Noise @ 1 MHz Offset	-83.5 dBc/Hz	-94.2 dBc/Hz
Current Draw on a 1.2 V supply	23 mA	13 mA
Figure of Merit	-173.7 dBc/Hz	-160.3 dBc/Hz

Phase noise of the VCO was estimated from the spectrum. Without the proper equipment to lock the signal, attempts at using the built-in phase noise personality of the spectrum analyzer would be invalid. The phase noise was conducted under battery power rather than a wall powered DC source to eliminate as much low frequency noise as possible. Measurements were conducted in a shielded room with large decoupling capacitors on all of the supply lines. The signal was measured at a resolution bandwidth of 300 kHz and a video bandwidth of 3 kHz to average out the free running oscillator bounce as best as possible. The measured value of the packaged VCO came to -83.5 dBc/Hz at 1 MHz offset, which matches very closely with simulation, but is almost a 10 dB degradation from the unpackaged circuit. The measurement was targeted to give an accurate estimate of phase noise at a 1 MHz offset. Figure 59 shows the measured packaged and unpackaged VCOs compared to their simulation counterparts. The measured phase noise of the unpackaged VCO actually outperforms the simulated values at 1 MHz offset, which may be an anomaly. The figure of merit for the packaged oscillator is calculated to be -160.16 dBc/Hz. This degradation from the unpackaged circuit is almost entirely caused by the change in phase noise measurement. Table VII summarizes the difference between the packaged and unpackaged circuit.

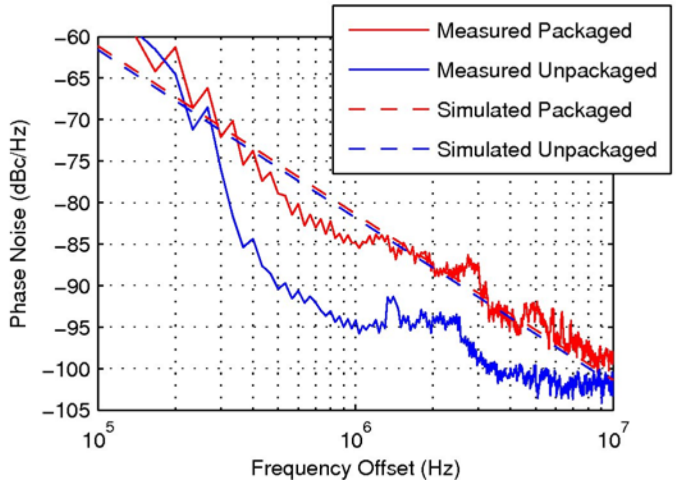

Fig. 59. Phase noise of the packaged and unpackaged VCO. The measurements were extrapolated from spectrum data measured at a resolution bandwidth of 300 kHz.

A mm-wave SiGe oscillator has been successfully packaged using an LCP organic material for the first time while maintaining a high performance profile. Measurements after packaging showed a figure of merit 13 dB down from the on chip measurements. Much of this degradation in the oscillator performance was expected due to the wire bond connections. This can be improved by decreasing the length of wire bonds or by using flip-chip bonding techniques. The next step to improve the package is to increase the LCP thickness creating a more flush surface between the VCO and transmission lines. This will allow a reduced length on all the wire bonds. This work paves the way for low cost mm-wave front ends combining Si devices with low temperature organic substrates

Publications

[1] N. Kingsley, D. Anagnostou, M. Tentzeris and J. Papapolymerou, "RF MEMS Sequentially-Reconfigurable Sierpinski Antenna on a Flexible, Organic Substrate without the Need for DC Bias Lines," *IEEE/ASME Journal of Microelectromechanical Systems*, Vol. 16, No. 5, pp. 1185-1192, October 2007

[2] N. Kingsley, S. Bhattacharya and J. Papapolymerou, "Moisture Lifetime Testing of RF MEMS Switches Packaged in Liquid Crystal Polymer," *IEEE Transactions on Components and Packaging Technologies,* Vol. 31, No. 2, pp. 345-350, June 2008.

[3] S. Nikolaou, N. Kingsley, G. Ponchak, J. Papapolymerou and M. Tentzeris, "UWB Elliptical Monopoles with a Reconfigurable Band Notch Using MEMS Switches Actuated Without Bias Lines," *IEEE Transactions on Antennas and Propagation,* Vol. 57, No. 8, pp. 2242-2251, August 2009.

[4] D. Chung, R. Polcawich, D. Judy, J. Pulskamp and J. Papapolymerou, "A Reduced Size Low Voltage RF MEMS X-Band Phase Shifter Integrated on Multilayer Organic Package," *submitted to IEEE Microwave and Wireless Component Letters*, January 2011.

[5] D. Chung, R. Polcawich, D. Judy, J. Pulskamp and J. Papapolymerou, "A SP2T and SP4T Switch Using Low Loss Piezoelectric MEMS," *2008 IEEE International Microwave Symposium*, pp. 21-24, Atlanta, GA, June 2008.

[6] C. Patterson, S. Horst, S. Bhattacharya, J. Cressler and J. Papapolymerou, "Low Cost Organic Packaging For Silicon Based mm-wave Wireless Systems," *2008 IEEE European Microwave Conference Digest*, Amsterdam, The Netherlands, October 2008.

Awards

Prof. John Papapolymerou was the co-recipient of the 2010 IEEE Antennas and Propagation Society *John Kraus Antenna Award* for the reconfigurable MEMS Sierpinski antenna.

Prof. John Papapolymerou was the recipient of the 2009 IEEE Microwave theory and Techniques Society Outstanding Young Engineer Award.